BNL-212005-2019-JAAM

Retrieval of high time resolution growth factor probability density function from a humidity-controlled fast integrated mobility spectrometer

Y. Wang,

To be published in "Aerosol Science and Technology"

June 2019

Environmental and Climate Sciences Department

Brookhaven National Laboratory

U.S. Department of Energy

USDOE Office of Science (SC), Basic Energy Sciences (BES) (SC-22)

DISCLAIMER

Retrieval of High Time Resolution Growth Factor Probability Density Function from a Humidity-controlled Fast Integrated Mobility Spectrometer

Yang Wang,[1,2] Guangjie Zheng,[1,2] Steven R. Spielman,[3] Tamara Pinterich,[1] Susanne Hering,[3] and Jian Wang[1,2 *]

[1]Environmental and Climate Sciences Department
Brookhaven National Laboratory
Upton, NY, 11973, USA

[2]Center for Aerosol Science and Engineering
Department of Energy, Environmental and Chemical Engineering
Washington University in St. Louis
St. Louis, MO, 63130, USA.

[3]Aerosol Dynamics Inc.
Berkeley, CA, 94710, USA

Revised Manuscript Submitted to:
Aerosol Science and Technology
AST-MS-2019-061.R1
May 29th, 2019

* To whom correspondence should be addressed:
Tel: +1-314-935-3362
E-mail address: jian@wustl.edu

Abstract

Hygroscopicity describes the tendency of aerosol particle to uptake water and is among the key parameters in determining the impact of atmospheric aerosols on global radiation and climate. A hygroscopicity tandem differential mobility analyzer (HTDMA) system is the most widely used instrument for determining the aerosol hygroscopic growth. Because of the time needed to scan the classifying voltage of the DMA, HTDMA measurement often requires a minimum of 30 min to characterize the particle hygroscopic growth at a single relative humidity for 5 to 6 different sizes. This slow speed is often inadequate for measurements onboard mobile platforms or when aerosols evolve rapidly. Recently, a humidity-controlled fast integrated mobility spectrometer (HFIMS) was developed for measuring the hygroscopic growth of particles. The measurement speed of the HFIMS is about one order of magnitude faster than that of the conventional HTDMA.

In this work, a data inversion routine is developed to retrieve the growth factor probability density function (GF-PDF) of particles measured by the HFIMS. The inversion routine considers the transfer functions of the upstream DMA and the downstream water-based fast integrated mobility spectrometer (FIMS), and derives the GF-PDF that reproduces the measured responses of the HFIMS. The performance of the inversion routine is examined using ambient measurements with different assumptions for the spectral shape of the particle GF-PDF (multimodal lognormal or piecewise linear). The influences of the data inversion parameters and counting statistics on the inverted GF-PDFs were further investigated, and an approach to determine the optimized inversion parameters is presented.

1. Introduction

Aerosol hygroscopicity is a key parameter for assessing the impact of atmospheric aerosols on the global radiation budget through direct interaction with solar radiation and modification of cloud properties (Koloutsou-Vakakis et al. 1998; Liu and Wang 2010; Mei et al. 2013). Both aerosol particle growth due to uptake of water vapor under sub-saturated conditions and formation of cloud droplets in supersaturated environments are strongly influenced by the aerosol hygroscopic properties (Swietlicki et al. 2008). Aerosol hygroscopicity in the sub-saturated regime is commonly measured with a hygroscopicity tandem differential mobility analyzer (HTDMA) system (Liu et al. 1978; Gasparini et al. 2006; Lopez-Yglesias et al. 2014; Oxford et al. 2019), in which aerosol particles with nearly uniform mobility sizes are first classified by an upstream differential mobility analyzer (DMA), and then humidified under elevated relative humidity (RH). The size distribution of the humidified particles is finally characterized by a downstream DMA and CPC using scanning mobility technique (Wang and Flagan 1990). The GF-PDF provides not only the hygroscopicity, but also the mixing state of aerosol particles (Gysel et al. 2009; Stolzenburg and McMurry 2008).

Measuring aerosol hygroscopicity with HTDMA is time-consuming. In order to fully characterize the size distribution of the humidified particles, the classifying voltage of the downstream DMA needs to be scanned over a wide range (Stolzenburg and McMurry 1988). In addition, as aerosol hygroscopicity is often strongly size-dependent, the above measurement needs to be repeated at representative sizes, typically five or more in the submicrometer range (Duplissy et al. 2009; Nilsson et al. 2009). As a result, a measurement cycle at a single RH typically requires a minimum of 30 min (e.g., Cerully et al. 2011). This measurement speed is

often inadequate for measurements onboard mobile platforms, such as research aircrafts. Even for ground-based deployments or laboratory studies, the slow speed may lead to substantial biases in measured hygroscopicity for aerosols with rapidly evolving properties (e.g., aerosols generated during combustion).

The recently developed humidity-controlled fast integrated mobility spectrometer (HFIMS) drastically improves the speed of aerosol hygroscopicity measurements (Pinterich et al. 2017b). The HFIMS consists of a differential mobility analyzer (DMA), a relative humidity (RH) control unit, and a water-based fast integrated mobility spectrometer (FIMS) operated in series. The water-based FIMS (Pinterich et al. 2017a) provides nearly instantaneous measurement (1 Hz) of aerosol mobility size distribution, just like a fast integrated mobility spectrometer (Kulkarni and Wang 2006a; b; Olfert et al. 2008; Olfert and Wang 2009; Wang et al., 2017; Wang et al. 2018), but the growth of particles is archieved using laminar flow water condensation methodologies (Hering and Stolzenburg 2005; Spielman et al. 2017) instead of the condensation of alcohol vapor. The use of water vapor enables independent control of RH in the mobility separation region, which cannot be achieved with alcohol vapors due to their lower mass diffusivity. By speeding up the size distribution measurement of RH-conditioned particles, the HFIMS significantly reduces the time needed to characterize the submicron aerosol hygroscopic properties (at five sizes) to less than three minutes in total. The accuracy of HFIMS measurements was also demonstrated by reproducing the growth factor of ammonium sulfate particles as a function of RH (Pinterich et al., 2017b).

Characterization of aerosol hygroscopic growth requires retrieval of the GF-PDF, which provides key information such as the mean growth factor (GF) of the size-selected aerosol particles, the fraction of particles in different GF ranges, and the spread of GF in each mode. Similar to the HTDMAs, the measurement signal of the HFIMS is an integral transform of the aerosol GF-PDF, together with the transfer functions of the upstream DMA and FIMS. Several approaches have been developed to derive the GF-PDF from HTDMA measurements (Stolzenburg and McMurry 2008; Gysel et al. 2009). Among them is the inversion that retrieves the GF-PDF using a complete HTDMA kernel. In this approach, the GF-PDF is derived by optimizing its parameters to minimize the residual between the measured and calculated responses (χ^2) of the HTDMA. Two widely used inversion algorithm are the TDMAfit developed by Stolzenburg and McMurry (1988) and TDMAinv developed by Gysel et al. (2009). The main difference between these two algorithms is that the TDMAfit assumes the GF-PDF as a superposition of multiple Gaussians, while the TDMAinv uses a piecewise linear (PL) function to describe the GF-PDF. The GF-PDF could also be approximated by a multimodal lognormal (ML) distribution, so that the data inversion could be simplified with lognormal forms (Stolzenburg and McMurry 2008).

In this study, we present a data inversion routine to derive GF-PDF from HFIMS measurements. The inversion routine takes into account the transfer functions of the DMA and FIMS, and allows different assumptions of GF-PDF spectral shape, including ML or PL GF-PDFs. The data inversion routine was evaluated by applying to measurements of ambient aerosols. The dependence of retrieved GF-PDFs on the assumed spectral shape is examined. The influence of counting statistics and data inversion parameters, including the number of HFIMS instrument

response diameter bins as well as the number of modes of ML GF-PDF or the number of growth factor bins of PL GF-PDF is also characterized.

2. Methods

A schematic diagram of the HFIMS is shown in Fig.1. The working principle and geometries of the HFIMS are detailed in Pinterich et al. (2017b). In this study, a Nafion exchanger was used to dry (RH<20%) the aerosol sample, and a radioactive neutralizer (Model 3077a, TSI Inc., Shoreview, MN, USA) was used to bring aerosol sample to steady-state charge distribution before it enters the HFIMS. The sample aerosol was subsequently classified by a Long DMA (Model 3081, TSI Inc.), humidity-conditioned by another Nafion exchanger (Perma Pure LLC, Lakewood, NJ, USA), and measured by the water-based FIMS to determine the size distribution of humidified particles. The sheath flow of the FIMS with desired RH was generated by mixing humid and dry particle-free air. To prevent change of particle sizes inside the FIMS, the RH of the FIMS aerosol and sheath flows were maintained at the same value. In the FIMS, the RH-conditioned particles were first spatially separated according to their mobility in a uniform electric field generated via two parallel plates. The separated particles then enter a grounded and supersaturated growth channel, where they grow to sizes that are detectable by a high-speed CCD camera (Falcon HG Series, Teledyne Dalsa Inc., Canada) when illuminated by a horizontal laser sheet (Spielman et al. 2017). Our previous study shows that the water-based FIMS can achieve a 100% detection efficiency for particles down to 8 nm (Pinterich et al., 2017a). An example image taken by the CCD camera is also shown in Fig. 1, where the bright continuous lines correspond the walls of the flow channel and the scattered dots present illuminated grown particles. In the image, the location of a particle on the *x*-axis (i.e., the direction of uniform

electric field) is determined by its electrical mobility, and the number of particles in each vertical size bin (along the *y*-axis) scales with the particle concentration, as detailed in Section 3.1. The CCD camera collects images at a frequency of 10 Hz, and particles within a mobility range of a factor of 10 are simultaneously detected (Kulkarni and Wang 2006a). Hence, the HFIMS system realizes near instantaneous (1 Hz) measurement of grown particle size distributions. We note that it may take a very long time (e.g. $>10^3$ s) for some highly viscous aerosols to reach equilibrium size, especially under low RH conditions (Bones et al., 2012). Similar to conventional HTDMA, the average transport times of particles from the inlet of Nafion exchanger (i.e., dryer) to the inlet of DMA, and from the inlet of the RH conditioner to the inlet of the FIMS are on the order of 10 seconds, which may not be sufficient for some highly viscous aerosol particles to reach equilibrium size.

In this study, the sample ($Q_{\mathrm{a,FIMS}}$) and sheath ($Q_{\mathrm{sh,FIMS}}$) flow rates of the FIMS were maintained at 0.30 and 15.1 l/min via a proportional solenoid valve (MKS Instruments, Rochester, NY, USA) and a critical orifice (O'Keefe Controls Co., Trumbull, CT, USA). This high sheath-to-aerosol flow ratio allows the RH of sample aerosol be further conditioned by the sheath flow for any minor mismatch between the sheath and aerosol RHs (Pinterich et al., 2017a). The upstream DMA was operated with a closed sheath flow loop, and the sheath ($Q_{\mathrm{sh,DMA}}$) and aerosol ($Q_{\mathrm{a,DMA}}$) flow rates were held constant at 13.5 and 1.35 l/min, respectively. Therefore, a nominal transfer function resolution of 10 was achieved by the DMA, similar to the upstream DMA in traditional HTDMA systems.

The hygroscopicity of ambient and ammonium sulfate aerosol particles under a RH of 85% were measured by the HFIMS, and the data were used to challenge the data inversion routine (elaborated in Section 3). Additional measurements of ammonium sulfate aerosols under a low RH (20%) were also carried out to confirm the accuracy of HFIMS sizing. The laboratory-generated aerosols in this study were produced by atomizing $(NH_4)_2SO_4$-water (1.5mM) solution. Particles of 35, 50, 70, 110, 165, and 250 nm were classified by the DMA and further measured by the water-based FIMS after humidity conditioning. The series of particle sizes were selected according to Duplissy et al. (2009), to maintain that the particle sizes increase with a ratio of approximately 1.5. In this study, the ambient aerosols were sampled outside the laboratory of Aerosol Dynamics Inc. (Berkeley, CA), and they were expected to be representative of urban aerosols, with composition influenced by local traffic and pollution.

3. HFIMS data inversion

This section presents the data inversion routine of the HFIMS measurement, which includes image processing, transfer theory of the HFIMS, derivation of GF-PDF, and the performance evaluation of the HFIMS inversion routine.

3.1. Image processing

The raw data collected by the HFIMS include images similar to the example shown in Fig. 1. The images were captured at a frequency of 10 Hz and collected into raw data files of one minute each. The MATLAB® image processing toolbox was used to extract the locations of flow channel walls and all particles from the images. To derive size information from the FIMS measurements, we introduce instrument response mobility (Z_p^*) following the same approach as

in Kulkarni and Wang (2006a) and Wang et al. (2017), namely, for a non-diffusing particle entering the FIMS along the central inlet flow streamline, the instrument response mobility Z_{p}^{*} at the *x*-*y* position where the particle is detected is the same as the particle mobility Z_{p}. The instrument response size (D_{p}^{*}) could also be defined, and is related to the instrument response mobility (Z_{p}^{*}) via the Stokes-Millikan equation

$$Z_{\mathrm{p}}^{*} = \frac{neC}{3\pi\mu D_{\mathrm{p}}^{*}} \tag{1}$$

where μ is the dynamic viscosity of the carrier gas, n is the number of charges carried by the particle, e is the elementary charge, and C is the Cunningham slip correction factor. At the exit of the FIMS mobility separator, each location in the *x*-axis corresponds to a specific instrument response mobility Z_{p}^{*} (Kulkarni and Wang 2006a), where

$$\frac{Z_{\mathrm{p}}^{*}}{Z_{\mathrm{p,max}}^{*}} = (1+\beta)(3\tilde{x}^{2} - 2\tilde{x}^{3}) - \frac{\beta}{2} \tag{2}$$

and

$$Z_{\mathrm{p,max}}^{*} = \frac{Q_{\mathrm{sh,FIMS}}}{b l_{\mathrm{s}} E_{x}}\left[\frac{2+\beta}{2}\right] \tag{3}$$

In Eqs. (1) and (2), $\tilde{x}$ ($\tilde{x} = \frac{x}{a}$, $0 < \tilde{x} < 1$) is the location of particles in the *x*-axis normalized by the gap between the parallel plates ($a = 0.91$ cm). $Z_{\mathrm{p,max}}^{*}$ is the maximum mobility that can be measured by the FIMS, which is determined by the aerosol-to-sheath flow rate ($\beta = \frac{Q_{\mathrm{a,FIMS}}}{Q_{\mathrm{sh,FIMS}}}$), sheath flow rate ($Q_{\mathrm{sh,FIMS}}$), width of the separator (b), length of the separator (l_{s}), and electric field strength across the parallel plate (E_x).

Due to the influence of the Brownian diffusion and the fact that particles enter the FIMS along different flow streamlines, particles with mobility of Z_{p} may not be detected with the same instrument response mobility. Therefore, the transfer function of the FIMS needs to be taken into account in the data inversion routine as shown in the following section. In order to avoid the edge effects of the electric and flow fields, and to maintain good mobility resolution, only particles detected within the viewing window (i.e., $0.2a < x < 0.8a$, $-3.5\ \mathrm{cm} < y < 3.5\ \mathrm{cm}$) were recorded and used for data inversion. Hence, under the setting of this study, this viewing window corresponds to instrument response mobilities between $0.096Z^*_{\mathrm{p,max}}$ ($x = 0.2a$) and $0.90Z^*_{\mathrm{p,max}}$ ($x = 0.8a$). For example, at a FIMS voltage of 1kV, aerosols with diameters between 44.1 and 159 nm are detected within the viewing window. This viewing window was then separated into multiple bins according to D^*_{p} with bin boundaries evenly distribute in the logarithmic scale along the *x*-axis. For the i^{th} ($i = 1, 2, 3, \dots, l$) D^*_{p} bin, $D^*_{\mathrm{p},i-\frac{1}{2}}$ and $D^*_{\mathrm{p},i+\frac{1}{2}}$ represent the lower and upper boundaries of the bin, and $D^*_{\mathrm{p},i} = \left(D^*_{\mathrm{p},i-\frac{1}{2}} \cdot D^*_{\mathrm{p},i+\frac{1}{2}}\right)^{\frac{1}{2}}$ is the geometric mean diameter of the size bin. Hence, the instrument response mobility (Z^*_{p}) of the i^{th} D^*_{p} bin could be calculated with Eq. (1). Using Eqs. (1-3), the geometrical locations of these bin boundaries ($\tilde{x}_{i-\frac{1}{2}}$ and $\tilde{x}_{i+\frac{1}{2}}$) could be determined, and the number of particles in each D^*_{p} bin (R_i) during any time interval (t) could be counted. This process is depicted in Fig. 2.

3.2. Transfer theory of the HFIMS

The response (particle count) of the i^{th} D^*_{p} bin of the HFIMS (R_i) is determined by the aerosol size distribution, DMA transfer function, GF-PDF, and FIMS transfer function, and can be

derived using the following approach. Let $n(D_{p1}) = \frac{dN}{dD_{p1}}$ denote the particle number size distribution at the inlet of the HFIMS, the number concentration of particles with diameters between D_{p1} and $D_{p1} + d(D_{p1})$ can be written as

$$dN = \frac{dN}{dD_{p1}} \times dD_{p1} = n(D_{p1})dD_{p1} \quad (4)$$

The number concentration of particles with diameters between D_{p1} and $D_{p1} + d(D_{p1})$ downstream of the DMA can be derived as

$$dN_{DMA} = \frac{Q_{a,DMA}}{Q_{s,DMA}} \eta_{chg}(D_{p1}) \eta_{p,DMA}(D_{p1}) \Omega_{DMA}(V_{DMA}, \tilde{Z}_{p1}) dN \quad (5)$$

where $Q_{a,DMA}$ and $Q_{s,DMA}$ are the aerosol inlet and outlet flow rates through the DMA (assumed to be equal since the DMA was operated in a closed loop), $\eta_{chg}(D_{p1})$ is the aerosol charging efficiency, $\eta_{p,DMA}(D_{p1})$ is the particle penetration efficiency through the DMA, and $\Omega_{DMA}(V_{DMA}, \tilde{Z}_{p1})$ is the transfer function of the DMA operated under the voltage of V_{DMA}. $\tilde{Z}_{p1}$ is the particle mobility (Z_{p1}) normalized by the centroid mobility corresponding to the DMA classifying voltage (Z^*_{p1}). The detailed expressions of the DMA transfer function are shown in the Supplemental Information. For simplicity, this study assumed the particles carry one charge only. Previous work suggests that when the aerosol size distributions is broad, as is for typical ambient atmospheric aerosols, the influence of multiple charging on hygroscopicity measurement may be small (Gysel et al. 2009). The influence of multiple charging on GF-PDF inversion for aerosols of representative size distributions will be a subject of future study. The number concentration of particles with diameters between D_{p2} and $D_{p2} + d(D_{p2})$ at the outlet of the conditioner can be written as

$$dN_{\mathrm{cond}} = dD_{\mathrm{p2}} \int_{D_{\mathrm{p1}}=0}^{D_{\mathrm{p1}}=\infty} \eta_{\mathrm{p,cond}}(D_{\mathrm{p2}}) c_{\mathrm{cond}}(D_{\mathrm{p2}}, D_{\mathrm{p1}}) dN_{\mathrm{DMA}} \quad (6)$$

where the integration considers all possible values of D_{p1}. $\eta_{\mathrm{p,cond}}(D_{\mathrm{p2}})$ is the penetration efficiency of the conditioned particles, assuming that the particle growth from D_{p1} to D_{p2} is instantaneous. $c_{\mathrm{cond}}(D_{\mathrm{p2}}, D_{\mathrm{p1}})$ is the particle growth factor probability density function (GF-PDF). $c_{\mathrm{cond}}(D_{\mathrm{p2}}, D_{\mathrm{p1}})dD_{p2}$ represents the probability of a particle with a dry diameter of D_{p1} growing to a size between D_{p2} and $D_{\mathrm{p2}} + dD_{\mathrm{p2}}$ following the RH conditioning (Gysel et al. 2009; Stolzenburg 1988; Stolzenburg and McMurry 2008). The GF-PDF satisfies $\int_{D_{\mathrm{p2}}=0}^{D_{\mathrm{p2}}=\infty} c_{\mathrm{cond}}(D_{\mathrm{p2}}, D_{\mathrm{p1}})dD_{\mathrm{p2}} = 1$. A normalized form of the GF-PDF ($c_{\mathrm{cond,n}}(g, D_{\mathrm{p1}})$) is also commonly used, where $g = D_{\mathrm{p2}}/D_{\mathrm{p1}}$ represent the growth factor. The normalized form of the GF-PDF satisfies that $c_{\mathrm{cond,n}}(g, D_{\mathrm{p1}})dg = c_{\mathrm{cond}}(D_{\mathrm{p2}}, D_{\mathrm{p1}})dD_{\mathrm{p2}}$, meaning $c_{\mathrm{cond}}(D_{\mathrm{p2}}, D_{\mathrm{p1}}) = \frac{1}{D_{\mathrm{p1}}} c_{\mathrm{cond,n}}(g, D_{\mathrm{p1}})$ and $\int_{g=0}^{g=\infty} c_{\mathrm{cond,n}}(g, D_{\mathrm{p1}})dg = 1$. Given the narrow size range of the DMA transfer function, when the upstream DMA was operated under a same voltage, the dependence of the GF-PDF on D_{p1} is neglected. Finally, inside the FIMS, due to influence of the FIMS transfer function, the FIMS response to particles with diameters between D_{p2} and $D_{\mathrm{p2}} + d(D_{\mathrm{p2}})$ in the i^{th} D_{p}^{*} bin during any time interval (t) is calculated by

$$dR_i = \frac{Q_{\mathrm{a,FIMS}} N_{\mathrm{F}}}{\dot{N}_{\mathrm{F}}} \eta_{\mathrm{p,FIMS}}(D_{\mathrm{p2}}) \eta_{\mathrm{det}}(D_{\mathrm{p2}}) \Omega_{\mathrm{FIMS},i}(Z_{\mathrm{p2}}) dN_{\mathrm{cond}} \quad (7)$$

In this equation, $Q_{\mathrm{a,FIMS}}$ is the aerosol inlet flow rate through the FIMS, N_{F} is the number of frames (images) being used to count dR_i, $\dot{N}_{\mathrm{F}}$ is the frame rate, $\eta_{\mathrm{p,FIMS}}$ is the particle penetration efficiency through the FIMS, and η_{det} is the detection efficiency of FIMS, which is nearly 100% for particles above 8 nm (Pinterich et al. 2017a). $\Omega_{\mathrm{FIMS},i}(Z_{\mathrm{p2}})$ is the transfer function of the i^{th}

D_{p}^{*} bin of the FIMS. The detailed expressions of the FIMS transfer function is given in the Supplemental Information.

By combining Eqs. (4-7) and further assuming that the efficiency parameters except for the DMA transfer function, FIMS transfer function, and GF-PDF are relatively constant in the non-zero size range of the DMA and FIMS transfer function, the theoretical response of the i^{th} D_{p}^{*} bin of the HFIMS can be derived as

$$R_{i,\mathrm{theo}} = \frac{Q_{\mathrm{a,FIMS}} N_{\mathrm{F}}}{\dot{N}_{\mathrm{F}}} \eta_{\mathrm{p,FIMS}}\left(D_{\mathrm{p2},i}^{*}\right) \eta_{\mathrm{p,cond}}\left(D_{\mathrm{p2},i}^{*}\right) \eta_{\mathrm{chg}}\left(D_{\mathrm{p1}}^{*}\right) \eta_{\mathrm{p,DMA}}\left(D_{\mathrm{p1}}^{*}\right) n\left(D_{\mathrm{p1}}^{*}\right) \times \iint \frac{1}{D_{\mathrm{p1}}} c_{\mathrm{cond,n}}\left(g, D_{\mathrm{p1}}\right) \Omega_{\mathrm{FIMS},i}\left(Z_{\mathrm{p2}}\right) \Omega_{\mathrm{DMA}}\left(V_{\mathrm{DMA}}, \tilde{Z}_{\mathrm{p1}}\right) dD_{\mathrm{p2}} dD_{\mathrm{p1}} \tag{8}$$

where $D_{\mathrm{p2},i}^{*}$ is geometric mean diameter of the i^{th} D_{p}^{*} bin of the FIMS, and D_{p1}^{*} is the mobility size corresponding to the centroid mobility of the DMA. Eq. (8) shows that the theoretical response of the HFIMS is determined by the double integral that contains the FIMS transfer function, DMA transfer function, and the GF-PDF. To simplify the derivation, we define this double integral $\iint \frac{1}{D_{\mathrm{p1}}} c_{\mathrm{cond,n}}\left(g, D_{\mathrm{p1}}\right) \Omega_{\mathrm{FIMS},i}\left(Z_{\mathrm{p2}}\right) \Omega_{\mathrm{DMA}}\left(V_{\mathrm{DMA}}, \tilde{Z}_{\mathrm{p1}}\right) dD_{\mathrm{p2}} dD_{\mathrm{p1}}$ as G. By assuming the efficiency parameters and size distribution are constant within the narrow non-zero mobility range of the DMA transfer function, we can simplify Eq. (5) to:

$$N_{\mathrm{DMA}} = \eta_{\mathrm{chg}}\left(D_{\mathrm{p1}}^{*}\right) \eta_{\mathrm{p,DMA}}\left(D_{\mathrm{p1}}^{*}\right) n\left(D_{\mathrm{p1}}^{*}\right) \left.\frac{dD_{\mathrm{p1}}}{d\tilde{Z}_{\mathrm{p1}}}\right|_{D_{\mathrm{p1}}^{*}} \times \int_{0}^{\infty} \Omega_{\mathrm{DMA}}\left(V_{\mathrm{DMA}}, \tilde{Z}_{\mathrm{p1}}\right) d\tilde{Z}_{\mathrm{p1}} \tag{9}$$

In a DMA, for both diffusing and non-diffusing particles, $\int_{0}^{\infty} \Omega_{\mathrm{DMA}}\left(V_{\mathrm{DMA}}, \tilde{Z}_{\mathrm{p1}}\right) d\tilde{Z}_{\mathrm{p1}}$ can be approximated by $Q_{\mathrm{a,DMA}}/Q_{\mathrm{sh,DMA}}$ (Stolzenburg, 1988). Hence, Eq. (8) can be further simplified to

$$R_{i,\mathrm{theo}} = \frac{Q_{\mathrm{a,FIMS}} N_{\mathrm{F}}}{\dot{N}_{\mathrm{F}}} \eta_{\mathrm{p,FIMS}}\left(D^*_{\mathrm{p2},i}\right) \eta_{\mathrm{p,cond}}\left(D^*_{\mathrm{p2},i}\right) \frac{Q_{\mathrm{sh,DMA}}}{Q_{\mathrm{a,DMA}}} \left.\frac{d\tilde{Z}_{\mathrm{p1}}}{dD_{\mathrm{p1}}}\right|_{D^*_{\mathrm{p1}}} N_{\mathrm{DMA}} G \tag{10}$$

For particles with sizes larger than 30 nm, the penetration efficiency through RH conditioner and the FIMS was calculated to be close to 1 (Gormley and Kennedy, 1949). Hence, $N_{\mathrm{DMA}} = N_{\mathrm{cond}}$, and according to the operation principle of the FIMS, the total number of particles detected by the CCD camera is related with the inlet aerosol concentration by

$$R_{\mathrm{tot}} = \frac{Q_{\mathrm{a,FIMS}} b_{\mathrm{view}} N_{\mathrm{F}}}{\dot{N}_{\mathrm{F}} b} N_{\mathrm{cond}} \tag{11}$$

R_{tot} is the total counts of particles detected within the FIMS viewing window, i.e., $R_{\mathrm{tot}} = \sum_i R_{i,\mathrm{meas}}$, where $R_{i,\mathrm{meas}}$ is the measured response of the i^{th} D^*_{p} bin of the FIMS. b_{view} and b are the length of the viewing area of the CCD-captured image and the length of the FIMS mobility separator, both along the *y*-axis. Therefore, the theoretical response of the i^{th} D^*_{p} bin of the HFIMS could be determined by

$$R_{i,\mathrm{theo}} = \frac{R_{\mathrm{tot}} b}{b_{\mathrm{view}}} \frac{Q_{\mathrm{sh,DMA}}}{Q_{\mathrm{a,DMA}}} \left.\frac{d\tilde{Z}_{\mathrm{p1}}}{dD_{\mathrm{p1}}}\right|_{D^*_{\mathrm{p1}}} G \tag{12}$$

3.3. Calculation of GF-PDF

The GF-PDF provides a complete description of aerosol hygroscopic growth and needs to be derived from HFIMS measurements. Similar to HTDMA measurements, the response of HFIMS is a double integral of the DMA transfer function, FIMS transfer function, and GF-PDF, therefore the GF-PDF cannot be calculated directly (Eq. (12)). An inversion routine is commonly used to derived GF-PDF from HTDMA data, which optimizes the shape of an assumed GF-PDF and minimize the residual (χ^2) between measured and theoretical response of HTDMA. The "best" GF-PDF is the one that could reproduce the measured response (R_i) with

the minimal χ^2. Particle GF-PDF can be represented as a multimodal lognormal (ML) distribution (Stolzenburg and McMurry 2008):

$$c_{\mathrm{cond,n}}(g, D_{\mathrm{p1}}) = \sum_{k=1}^{k=p} \frac{D_{\mathrm{p1}} f_{0,\mathrm{cond},k}}{D_{\mathrm{p2}} \sqrt{2\pi ln^2(\sigma_{\mathrm{cond},k})}} exp\left[-\frac{1}{2}\frac{(\ln(gD_{\mathrm{p1}}) - \ln(G_{\mathrm{cond},k} D_{\mathrm{p1}}))^2}{ln^2(\sigma_{\mathrm{cond},k})}\right] \quad (13)$$

where p is the number of modes, $f_{0,\mathrm{cond},k}$ ($k = 1,2, \ldots, p$) is the fractional weight of k^{th} lognormal mode ($\sum_k f_{0,\mathrm{cond},k} = 1$), and $G_{cond,k}$ and $\sigma_{\mathrm{cond},k}$ are the mean diameter growth (or shrinkage) factor and geometric standard deviation of the k^{th} lognormal mode, respectively. The approximation given by Eq. (13) is suitable when multiple modes are observed by the instrument downstream of the second DMA, and it straightforwardly describes the particle mixing state. However, it is reported that the convergence of fitting multiple modes may not be robust in cases of closely overlapped modes and shoulders, and the successful convergence may depend on the initial guess. To solve this problem, Gysel et al. (2009) developed the TDMAinv algorithm, which approximates GF-PDF as a piecewise linear (PL) function with non-zero probability density at pre-defined growth factor (g) values. In the PL GF-PDF, the growth factor range is divided into q sections that are equally spaced on a linear scale, with non-zero probability density values at the boundaries of each section except for the lower and upper limits of the growth factor range. Such a GF-PDF, having a bin resolution of q, is defined by $q - 1$ non-zero probability density values. By definition, the integral of the PL GF-PDF within the growth factor range is 1. The TDMAinv is more robust compared to other inversion methods and has been tested in a series of laboratory and field studies (Kecorius et al. 2017; Tan et al. 2013; Tritscher et al. 2011). However, it has been shown that the shape of the GF-PDF derived using the TDMAinv may oscillate strongly when a high bin resolution is chosen (Gysel et al. 2009).

Similar phenomena also happen if a high mode number is assumed when solving for the ML GF-PDFs.

Deriving particle GF-PDF from HFIMS measurements require similar approaches used in HTDMA data analysis. As the response of the i^{th} D_{p}^{*} bin of the HFIMS is given by Eq. (12), the GF-PDF (i.e., $c_{\text{cond}}(D_{\text{p2}}, D_{\text{p1}})$) can be derived by optimizing its parameters such that the measured responses of the HFIMS ($R_{i,\text{meas}}$) are reproduced by the calculated responses ($R_{i,\text{calc}}$), minimizing the residual

$$\chi^2 = \sum_{i=1}^{l} (R_{i,\text{calc}} - R_{i,\text{meas}})^2 \tag{14}$$

where $R_{i,\text{calc}}$ is obtained by Eq. (12) using the optimized GF-PDF.

The parameters that need to be optimized are the $3 \times p$ mode parameters ($f_{0,\text{cond},k}$, $G_{cond,k}$, and $\sigma_{\text{cond},k}$) of the ML GF-PDF, or $q - 1$ non-zero probability density values at pre-defined growth factors of the PL GF-PDF. In this study, for multi-lognormal representation, GF-PDF is the sum of p overlapping lognormal modes with parameters $f_{0,\text{cond},k}$, $G_{cond,k}$, and $\sigma_{\text{cond},k}$ ($k = 1,2, \dots, p$) in the range of 0 to 1.0, 0.9 to 2.0, and 1.01 to 1.30, respectively. The initial guesses of parameters are identical for all modes, with values of 0.5, 1.2, and 1.05 for $f_{0,\text{cond},k}$, $G_{cond,k}$, and $\sigma_{\text{cond},k}$, respectively. In the piecewise linear representation, GF-PDF was assumed to have $q - 1$ non-zero probability density values in the growth factor (g) range between 0.8 and 2.0. The initial guesses of all probability density values except for the upper and lower limits (0.8 and 2.0) are set to 1. The GF-PDFs for 50 and 165 nm ambient aerosol particles were calculated assuming ML shape ($p = 2, 3$) and PL shape ($q = 10, 20$) with a HFIMS D_{p}^{*} bin number of 32

($l = 32$) and compared in Section 4.1. In this study, the GF-PDFs were calculated with the trust-region-reflective method by the MATLAB® software.

3.4. Optimization of HFIMS inversion routine

Inverting the GF-PDFs from HFIMS data depends on several parameters, including the total number of HFIMS D_{p}^{*} bins (l) as well as the number of modes (p) of ML GF-PDF or the number of growth factor bins (q) of PL GF-PDF. One advantage of HFIMS is that the number of FIMS D_{p}^{*} bins can be straightforwardly varied after the measurements. For a given measurement, a large l results in reduced counts in each D_{p}^{*} bin, and therefore increased uncertainty due to low counting statistics. On the other hand, inversion using few D_{p}^{*} bin may not be able to sufficiently resolve the spectrum of GF-PDF, especially when there are closely spaced growth factor peaks. The number of modes (p) of ML GF-PDF or the number of growth factor bins (q) of PL GF-PDF should also be optimized to represent the actual shape of the GF-PDF while avoiding unreal oscillations described by Gysel et al. (2009).

The influence of l, p and q on the inverted GF-PDF under the impact of random errors is examined using a Monte Carlo approach that takes into account the impact of measurement counting statistics. The theoretical HFIMS response in each D_{p}^{*} bin is first calculated by assuming a pre-defined ML GF-PDF ($c_{\mathrm{cond,n,def}}(g, D_{\mathrm{p1}})$) using Eq. (13). The actual response of the HFIMS i^{th} D_{p}^{*} bin follows the Poisson distribution:

$$\boldsymbol{P}(\boldsymbol{x}) = \frac{\boldsymbol{R}_{\boldsymbol{i}}^{\boldsymbol{x}}}{\boldsymbol{x}!}\mathbf{exp}(-\boldsymbol{R}_{\boldsymbol{i}}) \tag{15}$$

where R_i is the theoretical response of the i^{th} D_{p}^* bin to the aerosol with the pre-defined GF-PDF, and $P(x)$ is the probability of the i^{th} D_{p}^* bin having a response of x (actual response). The Monte Carlo simulation generates 500 sets of HFIMS responses that follow the above Poisson distribution for each D_{p}^*. Based on each set of simulated responses, the GF-PDF is inverted with both the ML and PL shape assumptions ($c_{\text{cond,n,inv}}(g, D_{\text{p1}})$), then compared against the pre-defined GF-PDF at 13 growth factors evenly distributed between 0.8 and 2.0 (0.8, 0.9, 1.0, …, 2.0 correspond to $i = 1, 2, 3, \dots, 13$) using

$$\gamma^2 = \frac{1}{13}\sum_{i=1}^{13}(c_{\text{cond,n,inv}}(g_i, D_{\text{p1}}) - c_{\text{cond,n,def}}(g_i, D_{p1}))^2 \quad (16)$$

The dependence of γ^2 on l is examined first, to optimize the number of HFIMS D_{p}^* bins (or the averaged counts per bin) in data inversion. Three pre-defined GF-PDFs with one, two, and three modes were used, and the detailed mode parameters can be found in Table S1.

Then, γ^2 is calculated using different p and q values with the optimized number of HFIMS D_{p}^* bins to examine the impact of p and q on inverted GF-PDF. The values of p and q are optimized from the dependence of the smoothness of the inverted GF-PDF on the residue χ^2 calculated using Eq. (14) (i.e, "L-curve", Hansen and O'Leary 1993; Talukdar and Swihart 2003). Here, the smoothness of the inverted GF-PDF is approximated based on its absolute 2nd derivative values evaluated at 11 growth factors between 0.8 and 2.0 (0.8, 1.0, 1.1, …, 2.0 correspond to $i = 1, 2, 3, \dots, 13$) using

$$\xi = \sum_{i=2}^{12} \left| 2c_{\mathrm{cond,n,inv}}\left(g_i, D_{\mathrm{p1}}\right) - c_{\mathrm{cond,n,inv}}\left(g_{i+1}, D_{\mathrm{p1}}\right) - c_{\mathrm{cond,n,inv}}\left(g_{i-1}, D_{\mathrm{p1}}\right) \right| \quad (17)$$

where a lower smoothness corresponds to a larger ξ.

4. Results and Discussion

4.1. Hygroscopicity measurement of laboratory-generated and ambient aerosols

Laboratory-generated $(NH_4)_2SO_4$ and ambient particles of six different diameters (35, 50, 70, 110, 165, and 250 nm) were classified by the upstream DMA and the ratios between the mean particle diameter measured by the FIMS to the DMA centroid diameter ($\overline{D_{\mathrm{p2}}}/D_{\mathrm{p1}}^{*}$) was calculated. The testing processes are shown in Fig. 3 for atomized $(NH_4)_2SO_4$ particles and Fig. 4 for ambient aerosols. When DMA voltage is stepped to classify particles of a different diameter, the voltage of FIMS is varied accordingly such that RH-conditioned particles are detected within the viewing window (Figs. 3b and 4b). Figs. 3(a) and 4(a) show the normalized *x*-locations ($\tilde{x}$) of particles detected within the viewing window as a function of time, and the color of contour plot represents the number of particles detected in each location bin (defined similar to Fig. 2 except that the bin boundaries distribute evenly along the *x*-axis).

The locations of the humidified $(NH_4)_2SO_4$ particles remain in a narrow band, indicating an unperturbed size distribution under 85% RH when the DMA and FIMS voltages were maintained constant. Following the change of DMA and HFIMS voltages, the locations of the particles also changed in the HFIMS captured images, and it took approximately 10 s for the particle position to stabilize (i.e., system reached steady state). The mean growth factors ($\overline{D_{\mathrm{p2}}}/D_{\mathrm{p1}}^{*}$) of $(NH_4)_2SO_4$

particles ranged from 1.50 to 1.52 for particles with diameters between 35 nm and 250 nm, in agreement with previous measurements (Petters and Kreidenweis 2007, Lopez-Yglesias et al. 2014). Unlike the single-component $(NH_4)_2SO_4$ particles, the location distributions of humidified ambient particles were much broader (Fig. 4a). Due to the lower concentration of ambient aerosols, the particle counts detected in each location bin were also much lower compared to the laboratory-generated $(NH_4)_2SO_4$ particles. The lower particle counts led to increased noise of the calculated growth factors (Fig. 4c). Our previous study (Pinterich et al., 2017b) showed that the relative standard error of average growth factor derived from HFIMS measurement is proportional to the standard deviation of the humidified particle sizes, and inversely proportional to the mean humidified particle size and square root of total particle counts detected during the sample period. Therefore, under clean environments where the ambient particle concentration is low, a longer sampling time is needed to achieve the same precision of measured particle growth factor. The location distribution of the humidified ambient particles also shows a size dependence of aerosol mixing state. Particles with diameter larger than 110 nm showed two clear bands in the detected particle locations, indicating an external mixture of particles with different hygroscopicity. In contrast, for particles with diameter less than 70 nm, the detected position of humidified particles exhibited a broad single band. For the ambient aerosol, $\overline{D_{\mathrm{p2}}}/D_{\mathrm{p1}}^{*}$ increased from 1.1 to approximately 1.3 as the aerosol dry diameter increased from 35 to 250 nm. The sizing accuracy of the HFIMS was verified by maintaining a RH of 20% in the conditioner and water-based FIMS sheath flow, and the $\overline{D_{\mathrm{p2}}}/D_{\mathrm{p1}}^{*}$ values were between 0.98 and 1.02 (Fig. S2).

The GF-PDFs were derived using the 20-s HFIMS responses shown in Fig. 4. The GF-PDFs were inverted by assuming both multimodal lognormal (ML) and piecewise linear (PL) shapes, and with a FIMS D_{p}^{*} bin number of 32 ($l = 32$). Figures 5a and 5c show the average 20-s measured responses and calculated responses of the HFIMS at dry diameters of 50 and 165 nm. The theoretical responses of the HFIMS were calculated using the inverted ML and PL GF-PDFs ($p = 2, 3$ and $q = 10, 20$) shown in Figs. 5b and 5d. While the GF-PDFs of both ML and PL shapes can quantitatively reproduce the measured HFIMS responses, there are clear differences between the ML and PL GF-PDF.

The ML GF-PDF reproduces the measured HFIMS responses well with three overlapping lognormal distributions. The mode parameters derived by the data inversion routine are shown in Table S2, and the contribution of each mode is given by the $f_{0,\mathrm{cond},k}$ values. The ML GF-PDF with two modes may not adequately reproduce the responses of the HFIMS (R_i), especially when the measured response shows narrow peaks. For example, for dry particle diameter of 165 nm, the inverted ML GF-PDF with two modes leads to substantially lower R_i values near 200 nm (Fig. 5c). Similarly, the PL GF-PDF inverted with a higher bin resolution ($q = 20$) results in better agreement with measured R_i compared to that inverted with a lower bin resolution ($q = 10$). The PL GF-PDF inverted with the higher bin resolution of 20 generally agrees with the inverted ML GF-PDF with three modes, however, it also exhibits unrealistic oscillations at certain growth factor values, especially when R_i shows a broad distribution (Fig. 5b). This could be explained by the relatively large width of the DMA and FIMS transfer functions, which makes the integral (Eq. (12)) somewhat insensitive to the shapes of the GF-PDF (Gysel et al. 2009). As a result, the measured responses R_i, especially when it has a broad distribution, could

be reproduced even the inverted GF-PDF oscillates around the true GF-PDF values. As expected, the mean growth factors calculated from the inverted GF-PDFs (GF) are very similar for different values of p or q used, with a relative difference within 0.9% and 3.2% for 50 and 165 nm ambient aerosols, respectively (Table S3). However, a GF-PDF that has unrealistic oscillations may lead to incorrect interpretation of the aerosol mixing state and the fraction of each aerosol type. This highlights the need to optimize the value of parameters including l, p, and q such that an accurate GF-PDF can be retrieved. The optimization is discussed in Section 4.2.

For comparison, the GF-PDFs of the 165 nm $(NH_4)_2SO_4$ particles under 20% and 85% RH were also inverted with the ML and PL assumptions. The calculated R_i and inverted GF-PDFs are displayed in Fig. 6. As expected, the inverted GF-PDFs for $(NH_4)_2SO_4$ particles shows a single narrow peak due to homogeneous particle composition and therefore hygroscopicity. However, the reconstructed responses derived from the inverted PL GF-PDF may not agree well with the measured responses, especially when a lower GF-PDF bin resolution is used (e.g., q = 10 in Fig. 6a). This is a result of the binning method used in calculating PL GF-PDF, where the growth factor corresponding to the peak of the actual narrow GF-PDF may be located between the two bin boundaries. For this case, GF-PDFs inverted assuming lognormal spectral shape provides a better fit of measured R_i (Fig. 6a) because the width of the GF-PDF is not limited by the bin resolution in the growth factor range, but is a function of the mode geometric standard deviation.

4.2. Optimization of the GF-PDF data inversion parameters

The number of HFIMS D_{p}^{*} bin (l) directly determines the HFIMS response (R_i) and strongly influence the counting statistic for each D_{p}^{*} bin. The ML and PL GF-PDFs were inverted based on the simulated HFIMS responses using different values of l as described in Section 3.4, and compared against the pre-defined GF-PDFs. Three pre-defined GF-PDFs were used to challenge the data inversion algorithm, and the inverted ML GF-PDF was assumed to contain two modes ($p = 2$) and the PL GF-PDF was calculated with a bin resolution of 10 ($q = 10$). In addition, total particle counts (R_{tot}) of 50, 100, and 200 were assumed. For each R_{tot}, a larger value of l results in a lower average response per size bin ($\overline{R_l}$).

Fig. 7 shows that for each R_{tot} value, there exists an optimal range of D_{p}^{*} bin number l (and therefore average counts per D_{p}^{*} bin) that leads to overall low γ^2 for all three pre-defined GF-PDF. A larger l value above the range leads to higher γ^2, likely a result of low $\overline{R_l}$ and therefore poor counting statistics in each FIMS D_{p}^{*} bin. On the other hand, below the optimal range, γ^2 increases with decreasing l because the variation of GF-PDF cannot be adequately resolved from the HFIMS responses when detected particle are grouped in few size bins. This is particularly true for the pre-defined GF-PDF 2 that has two closely spaced narrow peaks. As counting statistics is closely related to particle counts, optimal l range varies with the total particle counts R_{tot} (Fig. 7), and is 16-23, 23-32, and 23-45 for R_{tot} of 50, 100, and 200, respectively.

The influences of the mode number (p) and bin resolution (q) on inverted GF-PDF were examined using the three pre-defined GF-PDFs with $l = 32$ and $R_{\mathrm{tot}} = 100$. Fig. 8 shows the variaton of the smoothness of the inverted GF-PDF (ξ) and the residual in R_{i}, χ^2, for different p and q values. The intial increase of p and q values from the lowest values leads to improved

agreements between the measured and calculated HFIMS responses, as indicated by a reduced χ^2. At the same time, ξ remained largely constant. This corresponds to a region where an increased resolution of the GF-PDF enhances the accuracy in data inversion (i.e., reduced χ^2). However, when p and q increases above certain values, χ^2 exhibits minor decrease or even increase in some cases, while ξ value rises significantly. This strong increase of ξ is a result of unrealistic oscillations of inverted GF-PDF (e.g., Fig.5b) that reduces its smoothness. In this region, while the increase of p or q might lead to slighly better agreements in the HFIMS response, the the inverted GF-PDFs show unrealistic oscillation and do not represent the actual distribution of growth factors. The variation of ξ with χ^2 exhibits a L-shaped curve, and the "corner" of the L-curve corresponds to the optimal GF-PDF solution. Such L-curve method has been applied in many inversion problems (e.g., Hansen and O'Leary 1993; Talukdar and Swihart 2003; Liu et al. 1999). The differences between inverted and the true (i.e., pre-defined) GF-PDFs (γ^2) are shown as the size of the symbols in Fig. 8, and the results confirm that statistcially, the corner of the L-curve represents the best solution of the GF-PDF. For the cases shown in Fig. 8, the optimal ranges of p and q are 2 to 4 and 10 to 15, respectively. Comparisons between the pre-defined GF-PDFs and the inverted GF-PDFs using the optimized p and q values are shown in Fig. 9, where p=2, q=10 for GF-PDF 1, p=3, q=15 for GF-PDF 2, and p=3, q=10 for GF-PDF 3. The results demonstrate that the inversion parameters derived from L-curve method could effectively reconstruct the GF-PDFs ranging from simple to complex spectral shapes. This optimization method may also be applied to the inversion of HTDMA meaurements (e.g., Gysel et al.,) and other aerosol meaurements such as size distribution measurement from a scanning mobility particle sizer, and the mass-size distribution from a centrifucal particle mass analyzer (CPMA), and these will be subjects of future studies.

5. Conclusion

In this study, a data inversion algorithm of HFIMS measurements is developed and evaluated. The HFIMS consists of a DMA, a RH control unit, and a water-based FIMS operated in series, and allows rapid measurements of aerosol hygroscopic growth of size-resolved aerosol particles. At each particle size, the measured responses of the HFIMS are an integral of DMA transfer function, FIMS transfer function, and aerosol growth factor probability density function (GF-PDF) that describes aerosol hygroscopic growth. As the GF-PDF cannot be solved directly, a data inversion routine is developed to retrieve GF-PDF that reproduces the measured responses of the HFIMS. The GF-PDFs with different spectral shape assumptions (multimodal lognormal shape and piecewise linear shape) were derived for 50 and 165 nm ambient aerosols. The derived GF-PDF depends on several parameters, including the number HFIMS instrument response diameter bins (l), the number of lognormal modes of ML GF-PDF (p), and the growth factor bin resolution of PL GF-PDF (q). The impact of these parameters on the inverted GF-PDF are examined using simulated GF-PDFs with different spectral shapes and HFIMS responses, considering the influence of counting statistics. We show that there exists an optimal range of FIMS D_{p}^{*} bin number l that should be used for the inversion of GF-PDF. The range varies with total number of particle counts detected by the HFIMS. An approach based on "L-curve" method is developed to identify optimal values of p and q that lead to statistically the best solution of GF-PDF. The data inversion routine, together with the approach to optimize the inversion parameters, allows robust retrieval of GF-PDF from HFIMS measurements, and therefore rapid characterization of particle hygroscopic growth of size-resolved particles.

Acknowledgements

This work is supported by the U.S. Department of Energy's Small Business Innovation Research Program under contract DE-SC0013103 and Small Business Technology Transfer Program under contract DE-SC0006312.

References:

Bones, D. L., Reid, J. P., Lienhard, D. M., Krieger, U. K. (2012). Comparing the mechanism of water condensation and evaporation in glassy aerosol. *Proc. Natl. Acad. Sci*. 109(29), 11613-11618.

Cerully, K., Raatikainen, T., Lance, S., Tkacik, D., Tiitta, P., Petäjä, T., Ehn, M., Kulmala, M., Worsnop, D., Laaksonen, A. (2011). Aerosol hygroscopicity and CCN activation kinetics in a boreal forest environment during the 2007 EUCAARI campaign. *Atmos. Chem. Phys*. 11:12369-12386.

Duplissy, J., Gysel, M., Sjogren, S., Meyer, N., Good, N., Kammermann, L., Michaud, V., Weigel, R., dos Santos, S. M., Gruening, C. (2009). Intercomparison study of six HTDMAs: results and recommendations. *Atmos. Meas. Tech*. 2: 363-378

Gasparini, R., Li, R. J., Collins, D. R., Ferrare, R. A., and Brackett, V. G. (2006). Application of aerosol hygroscopicity measured at the Atmospheric Radiation Measurement Program's Southern Great Plains site to examine composition and evolution, *J. Geophys. Res*., 111: D05S12.

Gormley, P. G. and Kennedy M. (1949). Diffusion from a stream flowing through a cylindrical tube. *Proc. Royal Irish Acad*., 52A:163-169.

Gysel, M., McFiggans, G., Coe, H. (2009). Inversion of tandem differential mobility analyser (TDMA) measurements. *J. Aerosol Sci*. 40:134-151.

Hansen, P. C. and D. P. O'Leary (1993). The use of the L-curve in the regularization of discrete ill-posed problems. *SIAM J. Sci. Comput*. 14(6): 1487-1503.

Hering, S. and Stolzenburg, M. (2005). A method for particle size amplification by water condensation in a laminar, thermally diffusive flow. *Aerosol Sci. Technol*. 39:428-436.

Kecorius, S., Ma, N., Teich, M., van Pinxteren, D., Zhang, S., Größ, J., Spindler, G., Müller, K., Iinuma, Y., Hu, M. (2017). Influence of biomass burning on mixing state of sub-micron aerosol particles in the North China Plain. *Atmos. Environ*. 164:259-269.

Koloutsou-Vakakis, S., Rood, M. J., Nenes, A., and Pilinis, C. (1998). Modeling of aerosol properties related to direct climate forcing, *J. Geophys. Res*. 103, 17009-17032

Kulkarni, P. and Wang, J. (2006a). New fast integrated mobility spectrometer for real-time measurement of aerosol size distribution: I. Concept and theory. *J. Aerosol Sci*. 37:1303-1325.

Kulkarni, P. and Wang, J. (2006b). New fast integrated mobility spectrometer for real-time measurement of aerosol size distribution: II. Design, calibration, and performance characterization. *J. Aerosol Sci*. 37:1326-1339.

Liu, B., Pui, D., Whitby, K., Kittelson, D., Kousaka, Y., McKenzie, R. (1978). The aerosol mobility chromatograph: a new detector for sulfuric acid aerosols. *Atmos. Environ*. (1967) 12:99-104.

Liu, Y., Arnott, W. P., & Hallett, J. (1999). Particle size distribution retrieval from multispectral optical depth: Influences of particle nonsphericity and refractive index. *J. Geophys. Res.* 104(D24), 31753-31762.

Liu, X. and Wang, J. (2010). How important is organic aerosol hygroscopicity to aerosol indirect forcing? *Environ. Res. Lett*. 5:044010.

Lopez-Yglesias, X. F., Yeung, M. C., Dey, S. E., Brechtel, F. J., Chan, C. K. (2014). Performance evaluation of the Brechtel Mfg. Humidified Tandem Differential Mobility Analyzer (BMI HTDMA) for studying hygroscopic properties of aerosol particles. *Aerosol Sci. Technol*. 48:969-980.

Mei, F., Setyan, A., Zhang, Q., and Wang, J. (2013). CCN activity of organic aerosols observed downwind of urban emissions during CARES, *Atmos. Chem. Phys*., 13, 12155-12169.

Nilsson, E., Swietlicki, E., Sjogren, S., Löndahl, J., Nyman, M., Svenningsson, B. (2009). Development of an H-TDMA for long-term unattended measurement of the hygroscopic properties of atmospheric aerosol particles. *Atmos. Meas. Tech*. 2:313-318.

Olfert, J., Kulkarni, P., Wang, J. (2008). Measuring aerosol size distributions with the fast integrated mobility spectrometer. *J. Aerosol Sci*. 39:940-956.

Olfert, J. and Wang, J. (2009). Dynamic characteristics of a fast-response aerosol size spectrometer. *Aerosol Sci. Technol*. 43:97-111.

Oxford, C., Rapp, C., Wang, Y., Kumar, P., Watson, D., Portelli, J., Sussman, E., Dhawan, S., Jiang, J. and Williams, B., 2019. Development and qualification of a VH-TDMA for the study of pure aerosols. *Aerosol Sci. Technol*., 53(2): 120-132.

Petters, M. and Kreidenweis, S. (2007). A single parameter representation of hygroscopic growth and cloud condensation nucleus activity. *Atmos. Chem. Phys.* 7:1961-1971.

Pinterich, T., Spielman, S., Hering, S., Wang, J. (2017a). A Water-based Fast Integrated Mobility Spectrometer (WFIMS) with enhanced dynamic size range. *Aerosol Sci. Technol*. 10: 1212-1222.

Pinterich, T., Spielman, S. R., Wang, Y., Hering, S., Wang, J. (2017b). A Humidity-Controlled Fast Integrated Mobility Spectrometer (HFIMS) for Rapid Measurements of Particle Hygroscopic Growth. *Atmos. Meas. Tech*. 10 4915-4925.

Spielman, S., Hering, S., Kuang, C., Wang, J. (2017). Preliminary Investigation of a Water-based Method for Fast Integrating Mobility Spectrometry. *Aerosol Sci. Technol*. 10: 1223-1230.

Stolzenburg, M. (1988). An ultrafine aerosol size distribution measuring system. Unviersity of Minnesota, Minneapolis, MN.

Stolzenburg, M. and McMurry, P. (1988). TDMAFIT user's manual. University of Minnesota, Department of Mechanical Engineering, Particle Technology Laboratory, Minneapolis:1-61.

Stolzenburg, M. and McMurry, P. (2008). Equations governing single and tandem DMA configurations and a new lognormal approximation to the transfer function. *Aerosol Sci. Technol*. 42:421-432.

Swietlicki, E., Hansson, H., Hämeri, K., Svenningsson, B., Massling, A., McFiggans, G., McMurry, P., Petäjä, T., Tunved, P., Gysel, M. (2008). Hygroscopic properties of submicrometer atmospheric aerosol particles measured with H-TDMA instruments in various environments – A review. *Tellus B* 60:432-469.

Talukdar, S. S. and M. T. Swihart (2003). "An improved data inversion program for obtaining aerosol size distributions from scanning differential mobility analyzer data." *Aerosol Sc. Technol*. 37(2): 145-161.

Tan, H., Yin, Y., Gu, X., Li, F., Chan, P., Xu, H., Deng, X., Wan, Q. (2013). An observational study of the hygroscopic properties of aerosols over the Pearl River Delta region. *Atmos. Environ*. 77:817-826.

Tritscher, T., Dommen, J., DeCarlo, P., Gysel, M., Barmet, P., Praplan, A., Weingartner, E., Prévôt, A., Riipinen, I., Donahue, N. (2011). Volatility and hygroscopicity of aging secondary organic aerosol in a smog chamber. *Atmos. Chem. Phys*. 11:11477-11496.

Wang, S. C. and Flagan, R. C. (1990). Scanning electrical mobility spectrometer. *Aerosol Sci. Technol*. 13:230-240.

Wang, J., Pikridas, M., Spielman, S. R., & Pinterich, T. (2017). A fast integrated mobility spectrometer for rapid measurement of sub-micrometer aerosol size distribution, Part I: Design and model evaluation. *J. Aerosol Sci.* 108, 44-55.

Wang, Y., Pinterich, T., Wang, J. (2018). Rapid measurement of sub-micrometer aerosol size distribution using a fast integrated mobility spectrometer. *J. Aerosol Sci.* 121:12-20.

Figure Captions:

Fig. 1 A schematic diagram of the HFIMS system.

Fig. 2 A schematic diagram showing the method for dividing the HFIMS D_{p}^{*} bins and counting particles in a HFIMS-captured image.

Fig. 3 (a) The responses of the HFIMS during the measurement of atomized $(NH_4)_2SO_4$ aerosols under a RH of 85%. The DMA voltages corresponded to dry particle sizes of 35, 50, 70, 110, 165, and 250 nm. (a) The normalized *x*-locations ($\tilde{x}$) of particles detected within the viewing window as a function of time. The color of the contour plot shows the number of particles detected in each location bin. (b) The voltages applied to the DMA and FIMS as a function of time. (c) The ratios between the mean particle diameter measured by the FIMS to the DMA centroid diameter ($\overline{D_{p2}}/D_{p1}^{*}$) as a function of time.

Fig. 4 (a) The responses of the HFIMS during the measurement of ambient aerosols under a RH of 85%. The DMA voltages corresponded to dry particle sizes of 250, 165, 110, 70, 50, and 35 nm. (a) The normalized *x*-locations ($\tilde{x}$) of particles detected within the viewing window as a function of time. The color of the contour plot shows the number of particles detected in each location bin. (b) The voltages applied to the DMA and FIMS as a function of time. (c) The ratios between the mean particle diameter measured by the FIMS to the DMA centroid diameter ($\overline{D_{p2}}/D_{p1}^{*}$) as a function of time.

Fig. 5 (a) and (c): Comparison between the HFIMS measured response ($R_{i,\mathrm{meas}}$) and calculated responses ($R_{i,\mathrm{calc}}$) for (a) 50 nm and (c) 165 nm ambient aerosols using the inverted ML and PL GF-PDFs. (b) and (d): Inverted ML and PL GF-PDFs at (b) 50 nm and (d) 165 nm by using 2 and 3 modes ($p = 2, 3$) for the ML GF-PDFs and 10 and 20 bins ($q = 10, 20$) for the PL GF-

PDFs. The data inversion uses 32 FIMS D_{p}^{*} bins ($l = 32$), but to focus on the sizes of interest, the *x*-axis does not cover all 32 bins.

Fig. 6 (a) and (c): Comparison between the HFIMS measured response and calculated responses for 165 nm $(NH_4)_2SO_4$ particles under 20% and 85% RH using the inverted ML and PL GF-PDFs. (b) and (d): Inverted ML and PL GF-PDFs at 20% RH (b) and 85% RH (d) by using 1 mode for the ML GF-PDFs and 10 and 20 bins for the PL GF-PDFs. The data inversion uses 32 FIMS D_{p}^{*} bins ($l = 32$), but to focus on the sizes of interest, the *x*-axis does not cover all 32 bins.

Fig. 7 Influence of average response per HFIMS D_{p}^{*} bin ($\overline{R}_{\iota}$) on the difference between inverted ML/PL GF-PDFs and pre-defined GF-PDFs (γ^2). Subplots (a), (b), and (c) correspond to R_{tot} of 50, 100, and 200. The corresponding number of HFIMS D_{p}^{*} bins (l) is labeled on the top *x*-axis. The inset figure in subplot (a) shows the shapes of the three pre-defined GF-PDFs, whose mode parameters are listed in Table S1. Each $\overline{R}_{\iota} - \gamma^2$ correlation curve uses the GF-PDF of the same color in the inset figure.

Fig. 8 L-shaped curves showing the influence of ML GF-PDF mode numbers (p) and PL GFPDF bin resolutions (q) on the residual of inversion (χ^2) and smoothness of the inverted GFPDFs (ξ). Subplots (a) and (b), (c) and (d), and (e) and (f) correspond to GF-PDFs (1, 2, and 3) quantified by parameters in Table S1, and each color corresponds to a parameter (p or q) used in data inversion. The size of the symbols represents the difference between the inverted and pre-defined GF-PDFs (γ^2) calculated by Eq. (16).

Fig. 9 Comparisons between the pre-defined GF-PDFs and inverted ML and PL GF-PDFs optimized by the L-curve method under the influence of random errors. The mode parameters of the three pre-defined GF-PDFs are listed in Table S1.

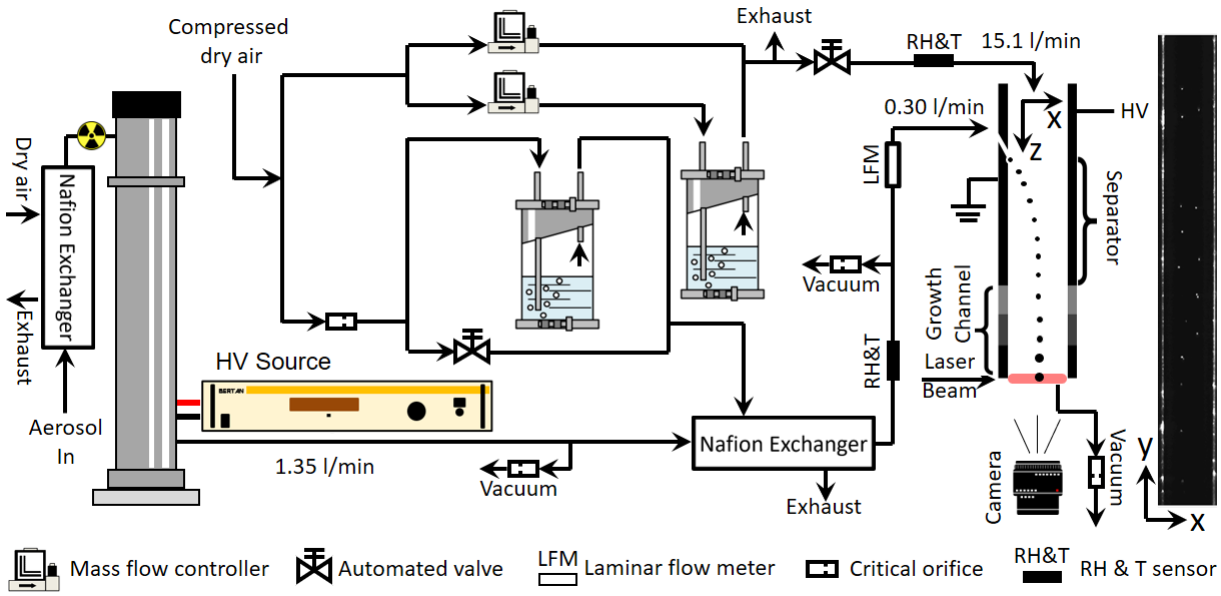
Compressed
dry air
Exhaust
RH&T
15.1 l/min
0.30 l/min
HV
X
Z
Separator
Dry air
Nafion Exchanger
Exhaust
LFM
Vacuum
Growth
Channel
Laser
Beam
RH&T
HV Source
Aerosol
In
1.35 l/min
Vacuum
Nafion Exchanger
Exhaust
Camera
Vacuum
y
x
Mass flow controller
Automated valve
LFM
Laminar flow meter
Critical orifice
RH&T
RH & T sensor

Fig. 1

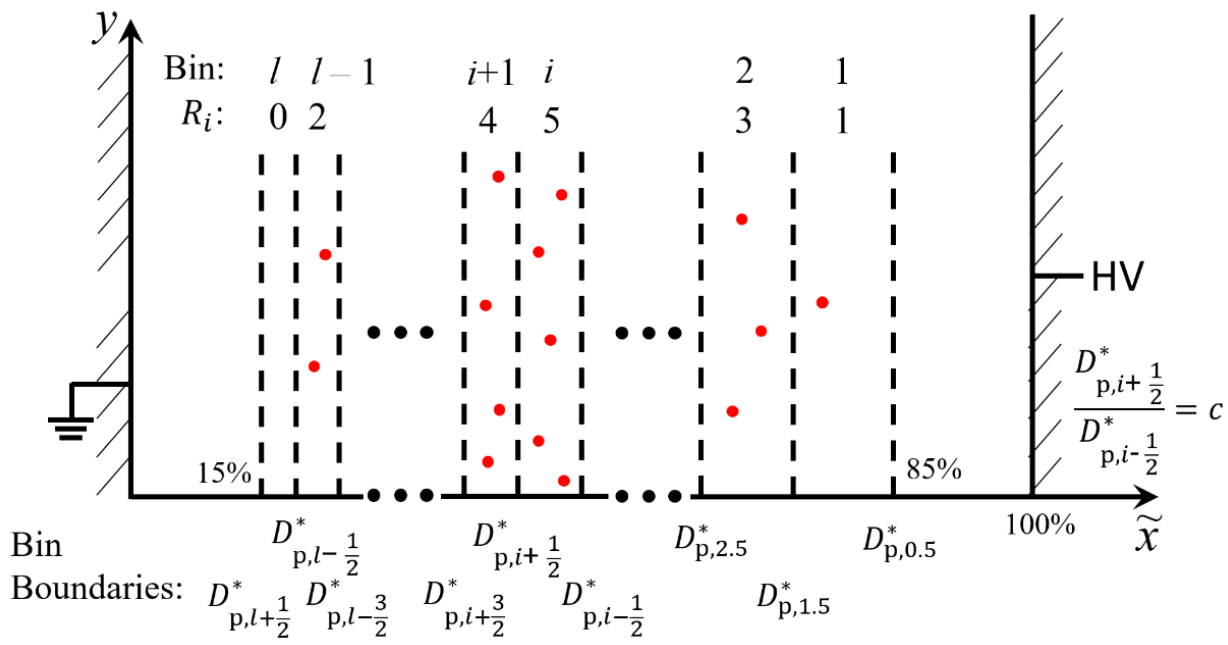
y
Bin: l l – 1 i+1 i 2 1
R_i: 0 2 4 5 3 1
HV
$\frac{D^*_{p,i+\frac{1}{2}}}{D^*_{p,i-\frac{1}{2}}} = c$
15%
85%
100%
$\tilde{x}$
Bin Boundaries:
$D^*_{p,l-\frac{1}{2}}$
$D^*_{p,i+\frac{1}{2}}$
$D^*_{p,2.5}$
$D^*_{p,0.5}$
$D^*_{p,l+\frac{1}{2}}$
$D^*_{p,l-\frac{3}{2}}$
$D^*_{p,i+\frac{3}{2}}$
$D^*_{p,i-\frac{1}{2}}$
$D^*_{p,1.5}$

Fig. 2

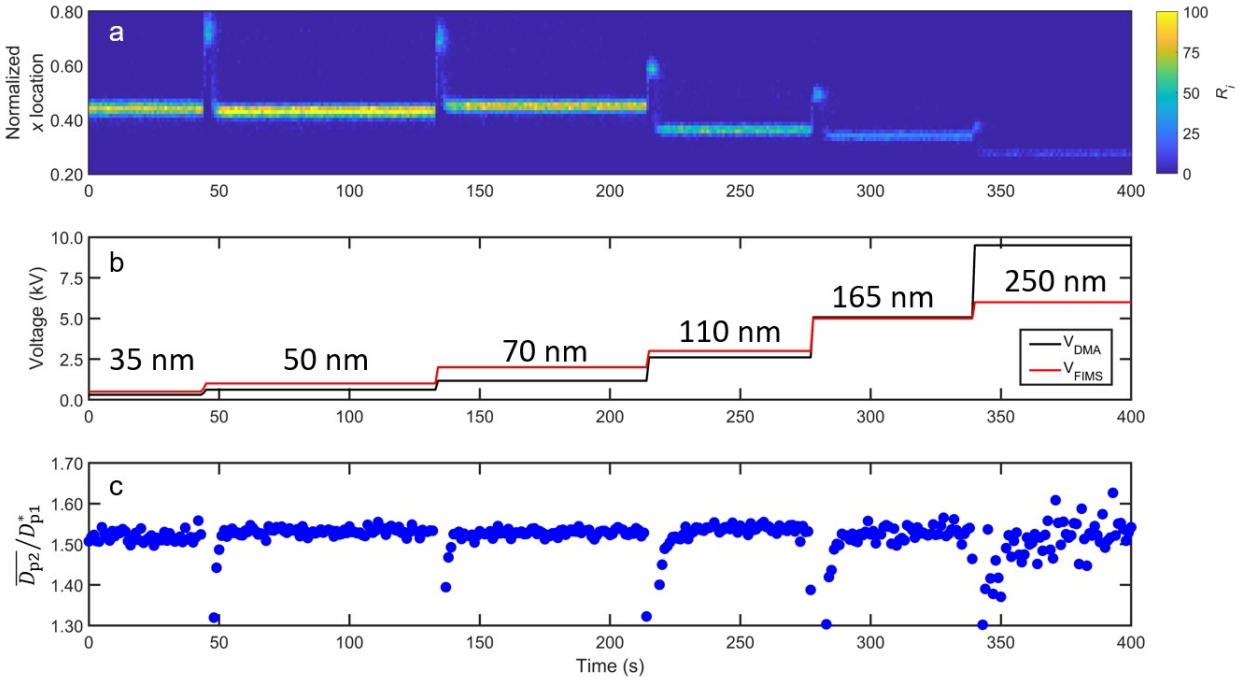
a
Normalized x location
0.80
0.60
0.40
0.20
0
50
100
150
200
250
300
350
400
100
75
50
25
0
R_i
b
Voltage (kV)
10.0
7.5
5.0
2.5
0.0
35 nm
50 nm
70 nm
110 nm
165 nm
250 nm
V_{DMA}
V_{FIMS}
c
$\overline{D_{p2}}/D_{p1}^{*}$
1.70
1.60
1.50
1.40
1.30
Time (s)

Fig. 3

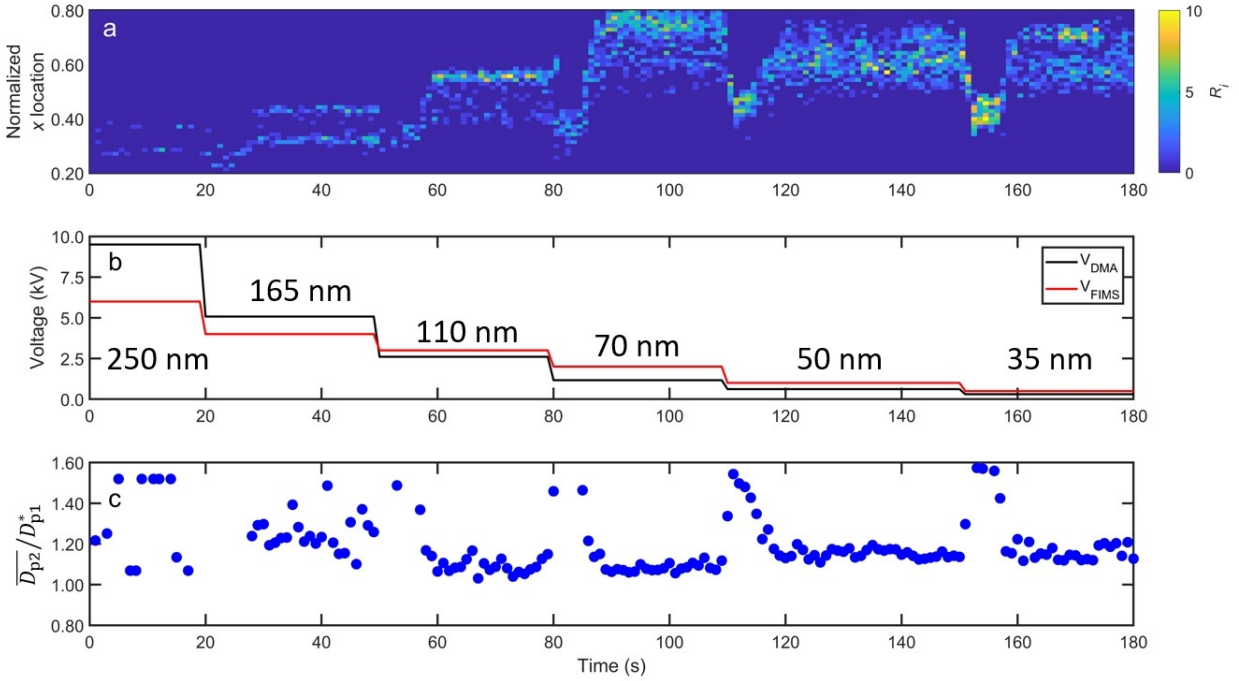
a
Normalized x location
0.80
0.60
0.40
0.20
10
5
0
R_i
b
Voltage (kV)
10.0
7.5
5.0
2.5
0.0
250 nm
165 nm
110 nm
70 nm
50 nm
35 nm
V_{DMA}
V_{FIMS}
c
$\overline{D_{p2}}/D_{p1}^*$
1.60
1.40
1.20
1.00
0.80
0
20
40
60
80
100
120
140
160
180
Time (s)

Fig. 4

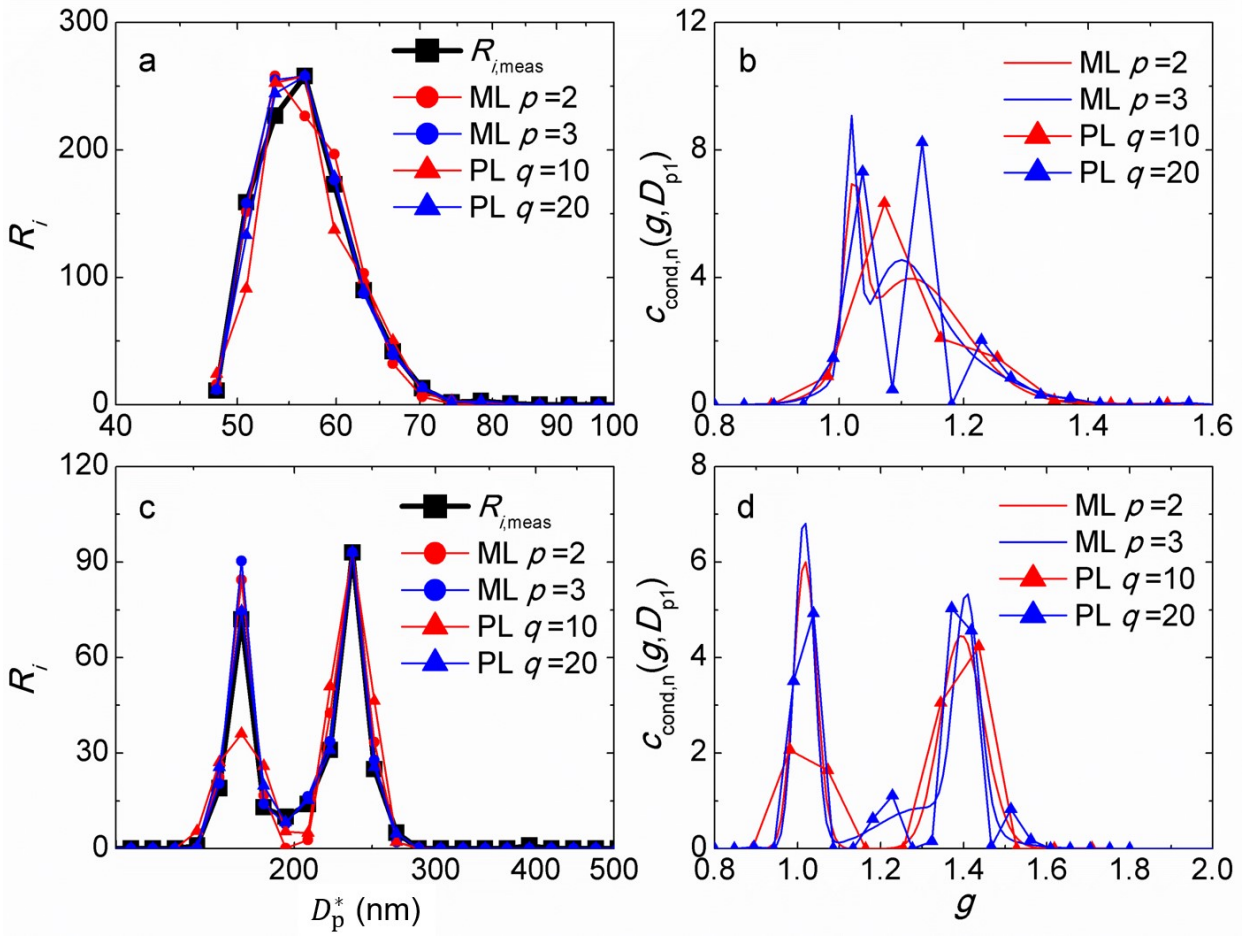
a
b
c
d
$R_{i,\mathrm{meas}}$
ML p =2
ML p =3
PL q =10
PL q =20
R_i
$c_{\mathrm{cond,n}}(g,D_{\mathrm{p1}})$
D_{p}^{*} (nm)
g

Fig. 5

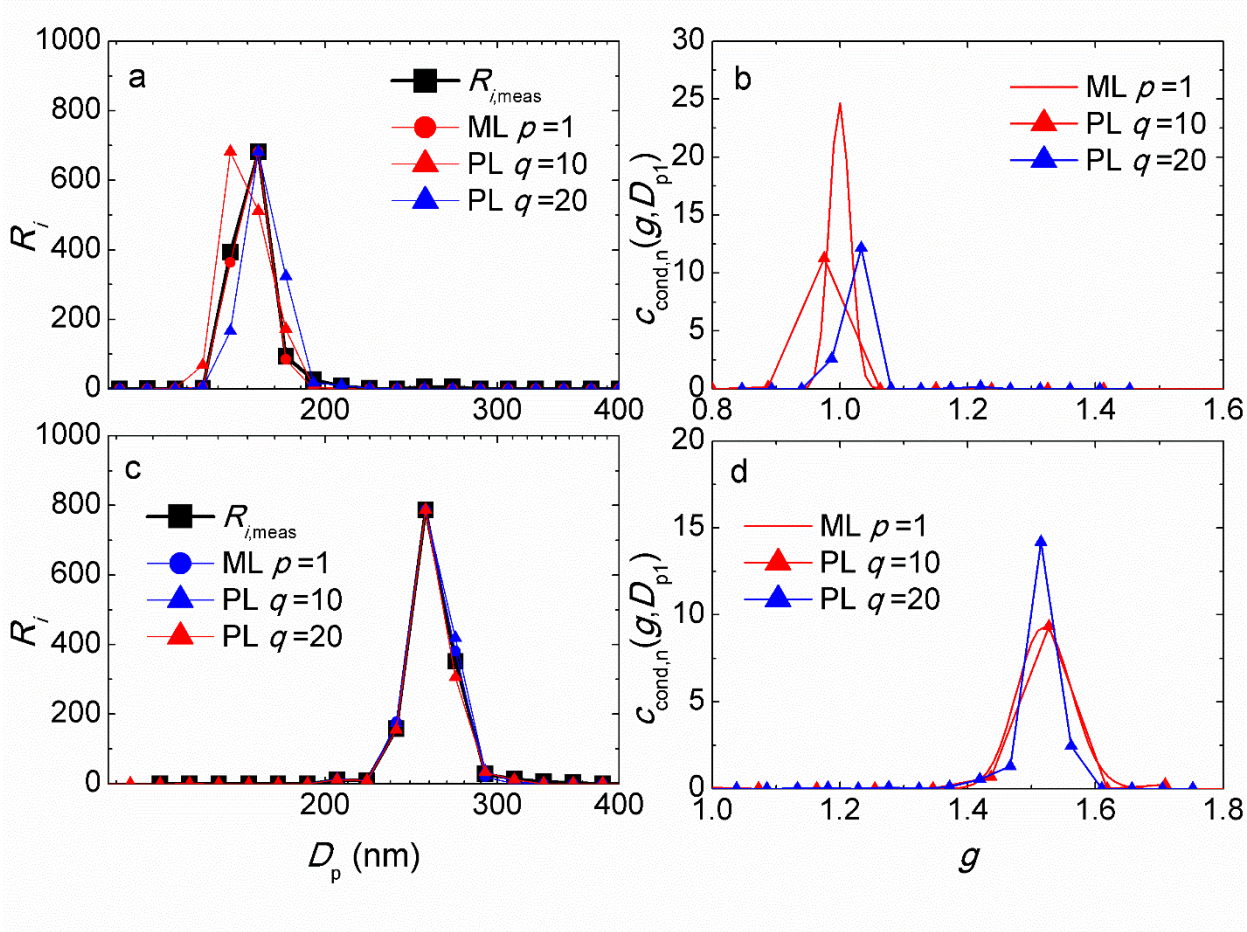
a
b
c
d
$R_{i,\mathrm{meas}}$
ML p=1
PL q=10
PL q=20
R_i
$c_{\mathrm{cond,n}}(g,D_{\mathrm{p1}})$
D_{p} (nm)
g

Fig. 6

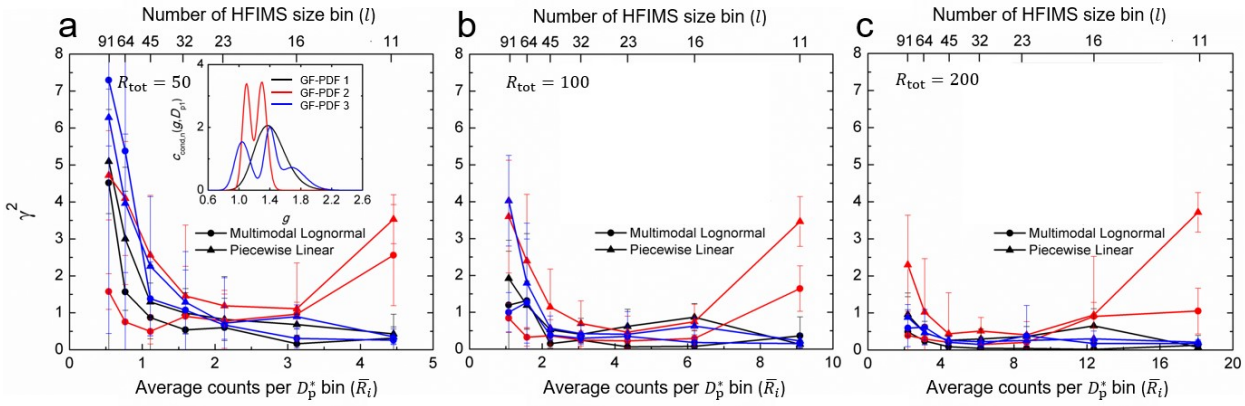
a
b
c
Number of HFIMS size bin (l)
91 64 45 32 23 16 11
$R_{\mathrm{tot}} = 50$
$R_{\mathrm{tot}} = 100$
$R_{\mathrm{tot}} = 200$
GF-PDF 1
GF-PDF 2
GF-PDF 3
$c_{\mathrm{cond},n}(g, D_{\mathrm{p}i})$
g
Multimodal Lognormal
Piecewise Linear
χ^2
Average counts per D_{p}^* bin ($\bar{R}_i$)

Fig. 7

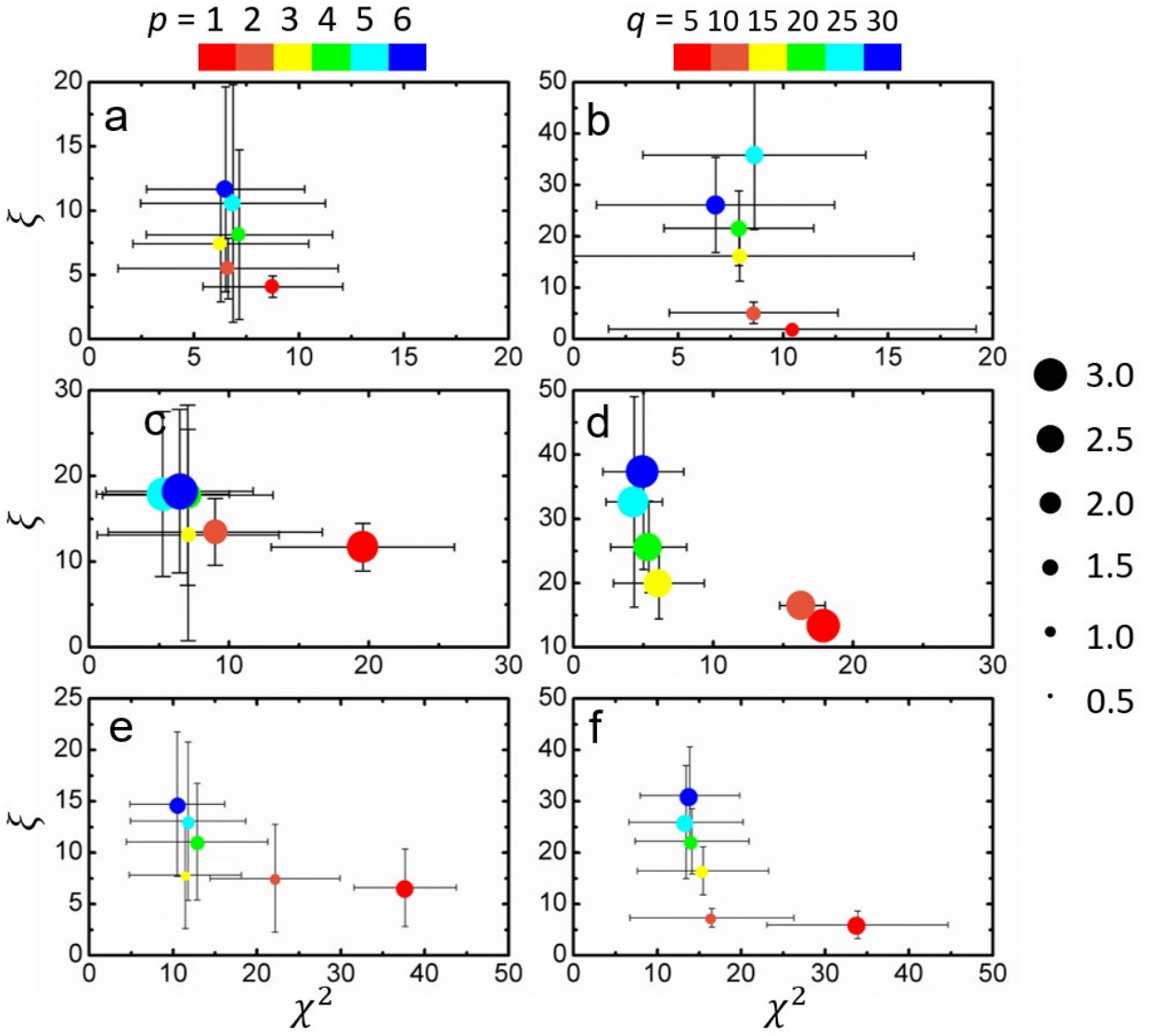

Fig. 8

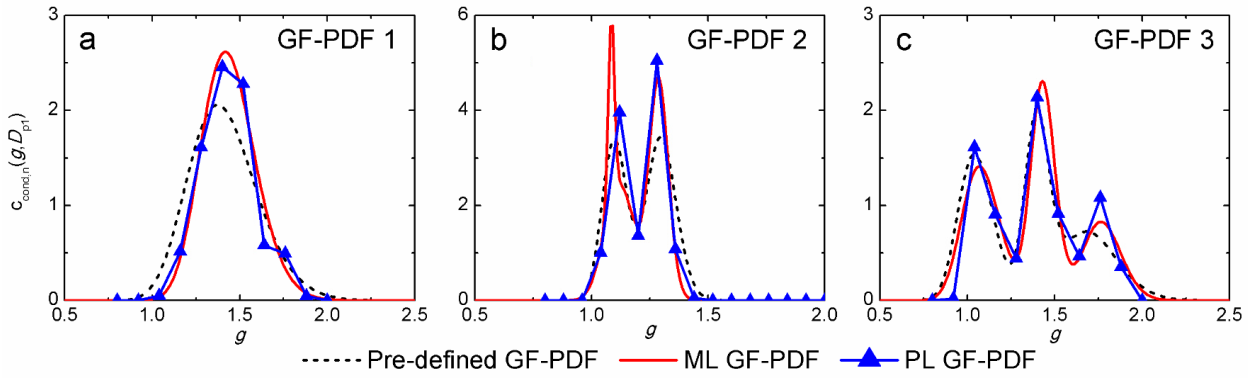
a
GF-PDF 1
b
GF-PDF 2
c
GF-PDF 3
$c_{cond,n}(g,D_{p1})$
g
Pre-defined GF-PDF
ML GF-PDF
PL GF-PDF

Fig. 9

Supplemental information for

Retrieval of High Time Resolution Growth Factor Probability Density Function from a Humidity-controlled Fast Integrated Mobility Spectrometer

Yang Wang,[1,2] Guangjie Zheng,[1,2] Steven R. Spielman,[3] Tamara Pinterich,[1] Susanne Hering,[3] and Jian Wang[1,2 *]

[1]Environmental and Climate Sciences Department
Brookhaven National Laboratory
Upton, NY, 11973, USA

[2]Center for Aerosol Science and Engineering
Department of Energy, Environmental and Chemical Engineering
Washington University in St. Louis
St. Louis, MO, 63130, USA.

[3]Aerosol Dynamics Inc.
Berkeley, CA, 94710, USA

Revised Manuscript Submitted to:
Aerosol Science and Technology
AST-MS-2019-061.R1
May 29th, 2019

* To whom correspondence should be addressed:
Tel: +1-314-935-3362
E-mail address: jian@wustl.edu

DMA and FIMS transfer functions

The DMA transfer function ($\Omega_{\mathrm{DMA}}(V_{\mathrm{DMA}}, Z_{\mathrm{p}})$) with and without particle diffusion has been solved by Stolzenburg (1988) via considering the particle movement across streamlines bounded by the inlet and outlet of the DMA. When particle diffusion is ignored,

$$\Omega_{\mathrm{DMA,nd}}(V_{\mathrm{DMA}}, Z_{\mathrm{p}}) = \frac{1}{2}\frac{1}{\Psi_2 - \Psi_1}\begin{bmatrix} -\left|\Psi_4 - \Psi_2 + Z_{\mathrm{p}}\Delta\Phi\right| + \left|\Psi_4 - \Psi_1 + Z_{\mathrm{p}}\Delta\Phi\right| \\ +\left|\Psi_3 - \Psi_2 + Z_{\mathrm{p}}\Delta\Phi\right| - \left|\Psi_3 - \Psi_1 + Z_{\mathrm{p}}\Delta\Phi\right| \end{bmatrix} \quad \text{(S1)}$$

and when particle diffusion is considered,

$$\Omega_{\mathrm{DMA}}(V_{\mathrm{DMA}}, Z_{\mathrm{p}}) = \frac{1}{\sqrt{2}}\frac{\sigma_{\Gamma,\mathrm{DMA}}}{\Psi_2 - \Psi_1}\begin{bmatrix} -\varepsilon\left(\frac{\Psi_4 - \Psi_2 + Z_{\mathrm{p}}\Delta\Phi}{\sqrt{2}\sigma_{\Gamma,\mathrm{DMA}}}\right) + \varepsilon\left(\frac{\Psi_4 - \Psi_1 + Z_{\mathrm{p}}\Delta\Phi}{\sqrt{2}\sigma_{\Gamma,\mathrm{DMA}}}\right) \\ +\varepsilon\left(\frac{\Psi_3 - \Psi_2 + Z_{\mathrm{p}}\Delta\Phi}{\sqrt{2}\sigma_{\Gamma,\mathrm{DMA}}}\right) - \varepsilon\left(\frac{\Psi_3 - \Psi_1 + Z_{\mathrm{p}}\Delta\Phi}{\sqrt{2}\sigma_{\Gamma,\mathrm{DMA}}}\right) \end{bmatrix} \quad \text{(S2)}$$

In these expressions, Ψ_1, Ψ_2, Ψ_3, and Ψ_4 are the stream functions at the boundaries of the DMA inlet and outlet slit. $\Delta\Phi$ is the difference between the electric flux functions at the DMA outlet and inlet, and $\sqrt{2}\sigma_{\Gamma,\mathrm{DMA}}$ is a measure of particle diffusion spreading along the particle streamline. $\varepsilon(x)$ is a function defined by

$$\varepsilon(x) = \int_0^x \mathrm{erf}(u)\,du = xerf(x) + \frac{1}{\sqrt{\pi}}e^{-x^2} \quad \text{(S3)}$$

Regarding the FIMS transfer function, by using a similar method to Stolzenburg (1988), the probability density function $P(Z_{\mathrm{p}}, \Psi_{\mathrm{out}})$, which dictates the probability of finding a particle with mobility Z_{p} that exits between streamlines Ψ_{out} and $(\Psi_{\mathrm{out}} + d\Psi_{\mathrm{out}})$, can be solved by (Kulkarni and Wang 2006a)

$$P_{\mathrm{FIMS,nd}}(Z_{\mathrm{p}}, \Psi_{\mathrm{out}}) = \frac{1}{2}\frac{1}{\Psi_{2,\mathrm{in}} - \Psi_{1,\mathrm{in}}}\begin{bmatrix} H(\Psi_{\mathrm{out}} - \Psi_{1,\mathrm{in}} - Z_{\mathrm{p}}\Delta\Phi) - \\ H(\Psi_{\mathrm{out}} - \Psi_{2,\mathrm{in}} - Z_{\mathrm{p}}\Delta\Phi) \end{bmatrix} \quad \text{(S4)}$$

when diffusion is ignored, and

$$P_{\mathrm{FIMS}}(Z_{\mathrm{p}},\Psi_{\mathrm{out}})=\frac{1}{2}\frac{1}{\Psi_{2,\mathrm{in}}-\Psi_{1,\mathrm{in}}}\left[\begin{matrix}\mathrm{erf}(\dfrac{\Psi_{\mathrm{out}}-\Psi_{1,\mathrm{in}}-Z_{\mathrm{p}}\Delta\Phi}{\sqrt{2}\sigma_{\Gamma,\mathrm{FIMS}}})-\\ \mathrm{erf}(\dfrac{\Psi_{\mathrm{out}}-\Psi_{2,\mathrm{in}}-Z_{\mathrm{p}}\Delta\Phi}{\sqrt{2}\sigma_{\Gamma,\mathrm{FIMS}}})\end{matrix}\right] \tag{S5}$$

when diffusion is considered (Kulkarni and Wang 2006a). In Eqs. (A.4) and (A.5), $\Psi_{1,\mathrm{in}}$ and $\Psi_{2,\mathrm{in}}$ are the stream functions at the lower and upper boundaries of the FIMS inlet, and $\sigma_{\Gamma,\mathrm{FIMS}}$ is determined by the spreading of particles due to diffusion. Note that Eqs. (A.4) and (A.5) are probability functions that work for point locations at the end of the mobility separator, where the point has a stream function of Ψ_{out}. In order to obtain the FIMS bin transfer function, regarding probability functions should be integrated within the FIMS bin, where

$$\Omega_{\mathrm{FIMS},i}(Z_{\mathrm{p}})=\int_{\Psi_{i-\frac{1}{2}}}^{\Psi_{i+\frac{1}{2}}}P(Z_{\mathrm{p}},\Psi_{\mathrm{out}})d\Psi_{\mathrm{out}} \tag{S6}$$

The integration limits are $\Psi_{i-\frac{1}{2}}$ and $\Psi_{i+\frac{1}{2}}$, corresponding to the bin boundary sizes of $D^{*}_{\mathrm{p},i-\frac{1}{2}}$ and $D^{*}_{\mathrm{p},i+\frac{1}{2}}$ shown in Section 3.1. Furthermore, due to the limited size of the viewing window of the CCD camera, the transfer function of the i^{th} bin of the FIMS can be solved by

$$\Omega_{\mathrm{FIMS},i,\mathrm{nd}}(Z_{\mathrm{p}})=\frac{1}{2}\frac{b_{\mathrm{view}}}{b}\frac{1}{\Psi_{\mathrm{in},2}-\Psi_{\mathrm{in},1}}\left[\begin{matrix}-\left|\Psi_{i+\frac{1}{2}}-\Psi_{\mathrm{in},2}+Z_{\mathrm{p}}\Delta\Phi\right|+\left|\Psi_{i+\frac{1}{2}}-\Psi_{\mathrm{in},1}+Z_{\mathrm{p}}\Delta\Phi\right|\\ +\left|\Psi_{i-\frac{1}{2}}-\Psi_{\mathrm{in},2}+Z_{\mathrm{p}}\Delta\Phi\right|-\left|\Psi_{i-\frac{1}{2}}-\Psi_{\mathrm{in},1}+Z_{\mathrm{p}}\Delta\Phi\right|\end{matrix}\right] \tag{S7}$$

when particle diffusion is ignored, and

$$\Omega_{\mathrm{FIMS},i}(Z_{\mathrm{p}})=\frac{1}{\sqrt{2}}\frac{b_{\mathrm{view}}}{b}\frac{\sigma_{\Gamma,\mathrm{FIMS}}}{\Psi_{\mathrm{in},2}-\Psi_{\mathrm{in},1}}\left[\begin{matrix}-\varepsilon\left(\dfrac{\Psi_{i+\frac{1}{2}}-\Psi_{\mathrm{in},2}+Z_{\mathrm{p}}\Delta\Phi}{\sqrt{2}\sigma_{\Gamma,\mathrm{FIMS}}}\right)+\varepsilon\left(\dfrac{\Psi_{i+\frac{1}{2}}-\Psi_{\mathrm{in},1}+Z_{\mathrm{p}}\Delta\Phi}{\sqrt{2}\sigma_{\Gamma,\mathrm{FIMS}}}\right)\\ +\varepsilon\left(\dfrac{\Psi_{i-\frac{1}{2}}-\Psi_{\mathrm{in},2}+Z_{\mathrm{p}}\Delta\Phi}{\sqrt{2}\sigma_{\Gamma,\mathrm{FIMS}}}\right)-\varepsilon\left(\dfrac{\Psi_{i-\frac{1}{2}}-\Psi_{\mathrm{in},1}+Z_{\mathrm{p}}\Delta\Phi}{\sqrt{2}\sigma_{\Gamma,\mathrm{FIMS}}}\right)\end{matrix}\right] \tag{S8}$$

when diffusion is considered. $\sigma_{\Gamma,\mathrm{DMA}}$ and $\sigma_{\Gamma,\mathrm{FIMS}}$ are dependent on the flow field in the DMA and FIMS, and the spreading of particle movement is different if different flow patterns are assumed. Note that the expressions in Eqs. (A.1-A.2) and Eqs. (A.7-A.8) are almost identical.

This is caused by the same mechanism of mobility separation in the DMA and FIMS, where the particle stream functions remain a constant along the trajectory of particles. Furthermore, each FIMS size bin can be regarded as an outlet slit similar to the configuration of the DMA. Hence, same expressions of transfer function can be used in FIMS. But since the flow patterns in the two instruments are different, detailed shapes of the DMA and FIMS transfer functions will vary.

Fig. S1 shows the actual shapes of the DMA (a) and FIMS (b) transfer functions. Owing to the longer residence time, Long DMA causes in considerable diffusion broadening of the transfer function. The shape of the FIMS transfer function, however, is distinct from that of the DMA. Ideal (non-diffusing) FIMS transfer functions possess trapezoidal shapes instead of triangular shapes. This phenomenon can be explained by drawing an analogy between FIMS and DMA, where the FIMS size bin can be considered as a DMA outlet. Triangular-shaped DMA transfer functions are obtained only when the aerosol inlet and outlet flow rate are equal ($Q_{\mathrm{s,DMA}} = Q_{\mathrm{a,DMA}}$). Because of the parabolic flow pattern in the FIMS and the method for dividing size bins, the aerosol flow rate through each size bin ($Q_{i,\mathrm{FIMS}}$) hardly matches exactly with the aerosol inlet flow rate ($Q_{\mathrm{a,FIMS}}$). This difference between $Q_{\mathrm{a,FIMS}}$ and $Q_{i,\mathrm{FIMS}}$ gives a trapezoidal shape of the FIMS transfer function, meaning particles within certain mobility ranges could exit the FIMS size bin with a same probability. In addition, unlike the DMA transfer function, where a non-diffusing transfer function works for all different sizes, the resolution of the non-diffusing FIMS transfer functions becomes lower as particle size becomes larger. This is caused by the higher relative uncertainties in measuring particles with smaller mobilities, where particles with smaller electrical mobilities (i.e., larger sizes, and theoretically can reach to infinitely large) concentrate in the aerosol stream near to the wall. At the same time, at locations near to the wall,

the difference between $Q_{\mathrm{a,FIMS}}$ and $Q_{i,\mathrm{FIMS}}$ becomes the largest as $Q_{\mathrm{a,FIMS}}$ approaches zero. This effect results in the similar lengths of the upper and lower bases in the trapezoidal-shaped transfer function, further deteriorating the resolution of the transfer function. To measure particles with larger sizes, the FIMS voltage can be raised accordingly, so that particles with larger inertial endure stronger electrostatic forces and move to the charged side of the parallel plate. Under a same voltage setting, the FIMS can measure particles spanning a factor of around three in particle diameter (a factor of 10 in mobility), which is sufficient to cover the entire range of growth factor for atmospheric aerosols at RH below 90%.

Table S1 Mode parameters of the pre-defined GF-PDFs for testing the data inversion algorithm.

Parameters	$f_{0,cond,k}$	$G_{cond,k}$	$\sigma_{cond,k}$
GF-PDF 1			
Mode 1	1.00	1.40	1.15
GF-PDF 2			
Mode 1	0.45	1.10	1.05
Mode 2	0.55	1.30	1.05
GF-PDF 3			
Mode 1	0.50	1.05	1.10
Mode 2	0.42	1.40	1.05
Mode 3	0.38	1.70	1.10

Table S2 Mode parameters of the multimodal lognormal GF-PDFs calculated for 50 and 165 nm ambient aerosols.

Parameters	$f_{0,cond,k}$	$G_{cond,k}$	$\sigma_{cond,k}$
	50 nm		
Mode 1	0.74	1.10	1.03
Mode 2	0.13	1.01	1.02
Mode 3	0.13	1.25	1.06
	165 nm		
Mode 1	0.39	1.01	1.02
Mode 2	0.36	1.42	1.03
Mode 3	0.26	1.25	1.13

Table S3 Mean growth factors of 50 and 165 nm ambient aerosols calculated by the first moment of the inverted GF-PDFs ($\mathrm{GF} = \int_{g=0}^{g=\infty} c_{\mathrm{cond,n}}(g, D_{\mathrm{p1}}) g dg$).

D_{p} (nm)	ML GF-PDF		PL GF-PDF	
	$p = 2$	$p = 3$	$q = 10$	$q = 20$
50	1.10	1.11	1.11	1.11
165	1.23	1.24	1.27	1.23

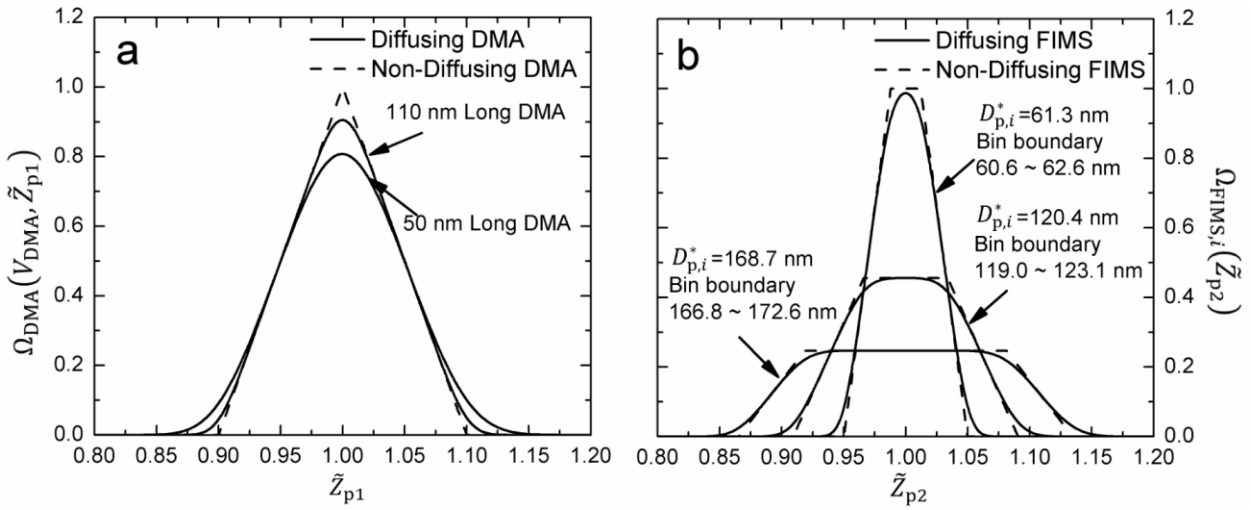

Fig. S1 (a) Normalized Long DMA transfer functions when classifying 50 and 100 nm particles at a sheath flow rate of 3 lpm and an aerosol flow rate of 0.3 lpm with and without particle diffusion; (b) Normalized FIMS transfer functions derived for different size bins with and without particle diffusion.

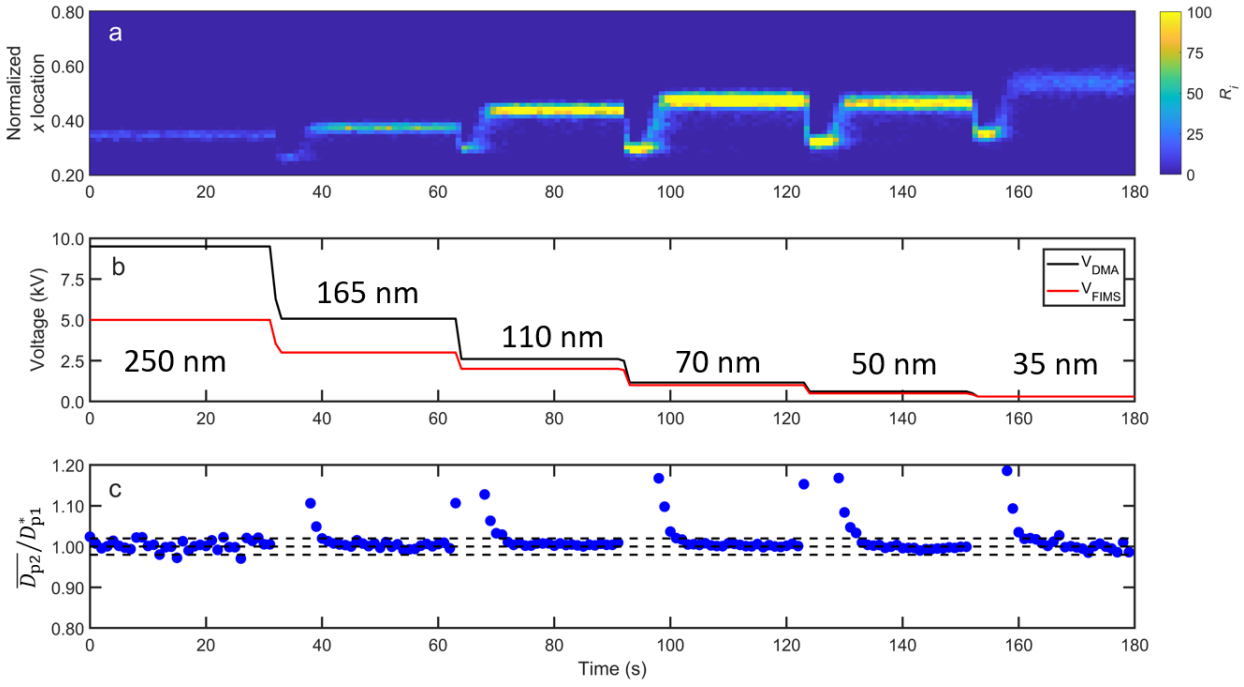

Fig. S2 The settings and response of HFIMS during the test of sizing accuracy. The sample aerosols were atomized $(NH_4)_2SO_4$ aerosols, and the DMA voltages corresponded to dry particle sizes of 250, 165, 110, 70, 50, and 35 nm. (a): The normalized x-locations ($\tilde{x}$) of particles detected in the viewing window as a function of time. The color of the contour plot shows the number of particles detected in each location bin. (b): The DMA and FIMS voltages as a function of time. (c): The ratios between the mean particle diameter measured by the FIMS to the DMA centroid diameter ($\overline{D_{p2}}/D^*_{p1}$) as a function of time. The dashed lines mark the growth factor of 0.98, 1.00 and 1.02.